Low-, medium-, and high-spin states in the N=Z+1 nucleus ^{63}Ga

Rudolph, D.; Ragnarsson, I.; Clark, R. M.; Andreoiu, C.; Carpenter, M. P.; Ekman, J.; Fahlander, C.; Kondev, F. G.; Lauritsen, T.; Sarantites, D. G.; Seweryniak, D.; Svensson, C. E.

Published in:
Physical Review C

DOI:
10.1103/PhysRevC.103.034306

2021

Document Version:
Publisher's PDF, also known as Version of record

Low-, medium-, and high-spin states in the $N = Z + 1$ nucleus ^{63}Ga

D. Rudolph,[1,*] I. Ragnarsson,[1] R. M. Clark,[2] C. Andreoiu,[1,3] M. P. Carpenter,[4] J. Ekman,[1,5] C. Fahlander,[1] F. G. Kondev,[4] T. Lauritsen,[4] D. G. Sarantites,[6] D. Seweryniak,[4] and C. E. Svensson[7]

[1]*Department of Physics, Lund University, S-22100 Lund, Sweden*
[2]*Nuclear Science Division, Lawrence Berkeley National Laboratory, Berkeley, California 94720, USA*
[3]*Chemistry Department, Simon Fraser University, Burnaby, British Columbia, V5A 1S6, Canada*
[4]*Physics Division, Argonne National Laboratory, Argonne, Illinois 60439, USA*
[5]*Department of Material Science and Applied Mathematics, Malmö University, S-20506 Malmö, Sweden*
[6]*Chemistry Department, Washington University, St. Louis, Missouri 63130, USA*
[7]*Department of Physics, University of Guelph, Guelph, Ontario, N1G 2W1, Canada*

(Received 27 September 2020; accepted 12 February 2021; published 5 March 2021)

The fusion-evaporation reaction ^{28}Si + ^{40}Ca at 122 MeV beam energy was used to populate excited states in the $N = Z + 1$ nucleus ^{63}Ga. With the combination of the Gammasphere spectrometer and the Microball CsI(Tl) charged-particle detector array, the level scheme of ^{63}Ga was extended by more than a factor of two in terms of number of γ-ray transitions and excited states, excitation energy ($E_x > 30$ MeV), and angular momentum ($I > 30\,\hbar$). Nine regular sequences of states were newly established in the high-spin part of the level scheme. The majority of these rotational band structures could be connected to the previously known part of the level scheme by high-energy γ-ray transitions in the energy range $E_\gamma = 4$–6 MeV. Low-spin states were assessed by shell-model calculations. The high-spin rotational bands were interpreted and classified by means of cranked Nilsson-Strutinsky calculations.

DOI: 10.1103/PhysRevC.103.034306

I. INTRODUCTION

The structure of nuclei located in the vicinity of the doubly magic nucleus ^{56}Ni can be expected to be described by the spherical shell model within the full $\mathcal{N} = 3$ fp model space, which comprises the $f_{7/2}$ orbital below, and the $p_{3/2}$, $f_{5/2}$, and $p_{1/2}$ orbitals above the $N = Z = 28$ shell gap. While this was found to be the case for low-spin states in mass $A \approx 50$–60 nuclei [1–5], the situation quickly becomes more complex for slightly heavier $N \approx Z$ nuclei and likewise as a function of excitation energy and angular momentum.

At high angular momenta, nuclei in the $A \approx 60$ region form rotational bands, based on holes in the $f_{7/2}$ orbitals and particles in the $g_{9/2}$ intruder orbitals [6,7]. Quadrupole deformation was found to increase with the number of particle-hole excitations across the shell gap and the number of particles placed in the $g_{9/2}$ intruder orbitals. This could be exemplified by the sequence of $N = Z$ nuclei [8], namely ^{56}Ni itself [9], ^{58}Cu [10], and ^{60}Zn [11]. Alternatively, the feature of increasing deformation with an increasing number of particles placed in the $g_{9/2}$ intruder orbitals could be delineated by means of comprehensive investigations of, for instance, ^{58}Ni [12], ^{59}Cu [13], ^{61}Cu [14], ^{61}Zn [15], or ^{62}Zn [16]. In all these cases, collective structures with varying numbers of holes in the $f_{7/2}$ orbitals and particles in the $g_{9/2}$ orbitals were observed and could be characterized for each nucleus.

At low spins, one expects the $N \approx Z$, $A \gtrsim 60$ nuclei to be governed by excitations and correlations within the upper fp shell, which can accommodate 12 protons and 12 neutrons, thus formally covering the region between ^{56}Ni and ^{80}Zr. However, it was both predicted and found experimentally that the proximity of the shape-driving $g_{9/2}$ orbital gives rise to a plethora of nuclear structure phenomena, which are enforced near the $N = Z$ line: collective octupole effects due to $p_{3/2}$-$g_{9/2}$ correlations in, for instance, $Z = 32$ germanium isotopes [17,18] and prolate-oblate shape coexistence [19–21] in $Z = 34$ selenium [22–24] or $Z = 36$ krypton isotopes [25,26].

The rapidly increasing influence of the $g_{9/2}$ shell in upper-fp nuclei also becomes evident from the presence of $I^\pi = 9/2^+$ (single-particle) states in odd-A nuclei, the excitation energy of which quickly decreases from ≈3.6 MeV in $A = 57$ [27,28] to ≈ 3.0 MeV in $A = 59$ [13], ≈ 2.5 MeV in $A = 61$ [13], and ⩽ 2.0 MeV in $A = 63$, 65, or 67 nuclei [29–31]. Similarly, $I^\pi = 7/2^-$ states are known in these nuclei, which call for $f_{7/2}^{-1}$ hole partitions. Therefore, a $fpg_{9/2}$ shell-model space is being called for, which could expand on, for instance, the $f_{5/2}pg_{9/2}$ space introduced in Ref. [32].

Last, odd-Z $N \approx Z$ isotopes are close to the proton dripline, which leads to observed (^{57}Cu) and anticipated (^{61}Ga

*Corresponding author: Dirk.Rudolph@nuclear.lu.se

[33]) proton radioactivity from low-lying, typically $I^\pi = 9/2^+$ states.

In the present work, a number of these nuclear structure topics are addressed in the study of the $N = Z + 1$ nucleus ^{63}Ga. Excited states in ^{63}Ga were first reported by Balamuth *et al.* based on a series of fusion-evaporation reaction experiments [29]. The analysis of $\gamma\gamma$ coincidences led to a proposed yrast sequence up to 7.7 MeV in excitation energy, E_x. Moreover, thorough angular-distribution and angular-correlation measurements were used to derive multipolarities of a number of γ-ray transitions in the low-energy part of the level scheme [29,34,35]. This allowed for tentative spin-parity assignments of a number of states, starting from the $I^\pi = 3/2^-$ ground state of ^{63}Ga [34,35]. More recently, the $I = 3/2$ ground-state assignment was determined by collinear laser spectroscopy of the series of gallium isotopes [36]. The level scheme of ^{63}Ga was later extended to $E_x \approx 14$ MeV and $I \approx 20\,\hbar$ in the high-spin study presented by Weiszflog *et al.* [30]. Earlier work was confirmed, including the multipolarity assignments of low-lying γ rays. Two consecutive γ rays were exchanged for two cascades due to improved sensitivity and the observation of parallel decay branches. Total Routhian surface calculations suggested triaxial shapes ($\beta_2 \approx 0.25$, $\gamma \approx 20^\circ$) of the band structures proposed in the $E_x \approx$ 6- to 14-MeV region [30].

More recently, an attempt to study the low-spin mirror symmetry of ^{63}Ga and ^{63}Ge was undertaken by means of few-nucleon knockout reactions [37]. Concerning ^{63}Ga, a few more weak transitions were found connecting the low-spin negative-parity states as suggested in Ref. [30].

Based on data from an experiment briefly described in Sec. II, and analysis methods briefly summarized in Sec. III, we report new experimental information on high-spin states in ^{63}Ga in Sec. IV. Shell-model and cranked Nilsson-Strutinsky calculations (CNS), used in the interpretation of the level scheme, are described in Sec. V. The shell-model calculations were applied to the interpretation of the low- and medium-spin regimes. The CNS calculations were used to interpret and classify the experimentally revised medium-spin structures as well as the newly observed, well-deformed bands beyond $E_x \gtrsim 15$ MeV and $I \gtrsim 20\,\hbar$. A brief summary concludes the paper.

II. EXPERIMENT

The experiment was conducted at the Argonne Tandem Linac Accelerator System (ATLAS). The fusion-evaporation reaction ^{28}Si + ^{40}Ca, at a beam energy of 122 MeV, was used to populate high-spin states in neutron-deficient, mass $A \approx 60$ nuclei near the $N = Z$ line [12–16,38]. Excited states in ^{63}Ga were reached following the evaporation of one α particle and one proton, i.e., the $1\alpha 1p$ reaction channel. An experimental relative production cross section of $\sigma_{\rm rel} \approx 0.5\%$ could be estimated from relative yields of known γ rays attributed to the various reaction channels. The ^{40}Ca target, enriched to 99.975%, was 0.5 mg/cm^2 thin. It was enclosed by two thin gold layers and transported to the target chamber in argon atmosphere to prevent oxidation.

The main instrument used in the experiment was the Gammasphere array [39], which comprised 101 germanium detector modules at the time. To enable γ-ray multiplicity and γ-ray sum-energy measurements [40], the heavimet collimators were removed from the germanium detector modules. Gammasphere surrounded the target chamber, and inside this chamber the nearly 4π 95-CsI(Tl)-element charged-particle detector system Microball [41] surrounded the ^{40}Ca target. Microball recorded energies and directions of evaporated charged particles, and pulse-shape analysis techniques allowed to discriminate between evaporated protons and α particles. The summed energies of the evaporated particles were correlated with the γ-ray multiplicity and γ-ray sum-energy information from Gammasphere, which aided reaction channel selection later [42]. Events were recorded when at least four Compton-suppressed γ rays were detected.

III. DATA ANALYSIS

The data analysis follows procedures which have been outlined previously in connection with similarly extensive studies of neighboring nuclei for this and similar experiments in the mass $A \approx 60$ region [12–16,38]. The momenta of the recoiling residues can be derived on an event-by-event basis using the energies and momenta of the evaporated charged particles measured with Microball. Since Gammasphere contains a number of twofold segmented germanium detectors around central angles, it is possible to perform more accurate Doppler-shift corrections and thus significantly improve γ-ray energy resolution.

In total, more than 20 different residual isotopes are produced in this type of fusion-evaporation reaction. ^{63}Ga represents a rather weakly populated channel of low particle multiplicity: $1\alpha 1p$. Thus, due to finite detection efficiencies for protons or α particles in Microball, a plain $1a1p$-coincidence requirement is not sufficient. The reason is that γ rays from much more intensely populated reaction channels would completely dominate the weak γ-ray transitions stemming from ^{63}Ga, preventing a meaningful work on the level scheme of ^{63}Ga. By missing the detection of one or two protons or one α particle, the main contributors to the $1\alpha 1p$ spectra are ^{62}Zn ($1\alpha 2p$ [16]), ^{61}Cu ($1\alpha 3p$ [14]), or ^{59}Cu ($2\alpha 1p$ [13]). The solution is to implement strict conditions on the total-energy and γ-ray multiplicity selection mentioned earlier [40,42].

As a first step, the total-energy selection provides γ-ray analysis objects (see below) with a considerably improved ratio of ^{63}Ga:^{62}Zn $\approx$ 1 : 10, as well as being essentially free from γ rays from other reaction channels. Second, it turns out that a number of key γ-ray transitions in the known yrast sequence of ^{63}Ga [29,30] (cf. Fig. 1) are not significantly obscured by γ-ray transitions known to belong to ^{62}Zn [16]. Thus, a γ-ray coincidence requirement with any of the 75-, 625-, 649-, 894-, 1077-, or 1140-keV transitions can be used to very selectively tag ^{63}Ga. Adding in modest background from ^{62}Zn but significantly increasing statistics for the ^{63}Ga analysis, this list of ^{63}Ga transitions can be expanded with those at 1209, 1330, 1422/1425, 1632/1635, and 1772 keV, thus representing essentially the full yrast sequence between the 9040-keV $31/2^{(-)}$ state and the ground state of ^{63}Ga (cf. Fig. 1).

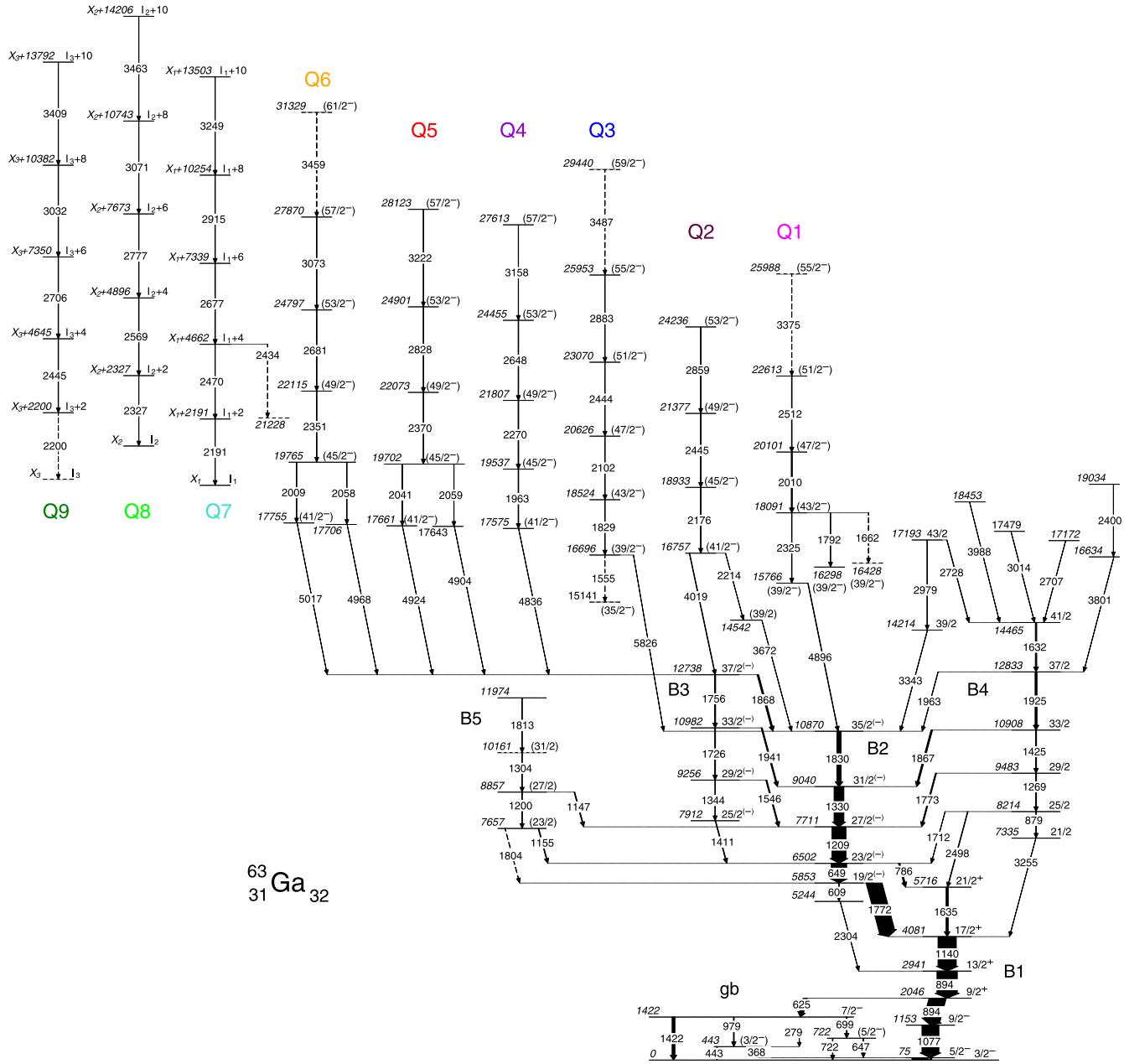

FIG. 1. Proposed high-spin level scheme of ^{63}Ga from the present study. Energy labels are in keV. Tentative transitions and levels are dashed. The widths of the arrows correspond to the relative intensities of the γ rays. Based on intensity pattern and decay-out characteristics, the bands labeled Q7, Q8, and Q9 have been tentatively placed at $X_1 = 19\,000$ keV with $I_1 = (43/2)$, $X_2 = 20\,300$ keV with $I_2 = (45/2)$, and $X_3 = 19\,200$ keV with $I_3 = (43/2)$, respectively.

With the $1\alpha 1p$ coincidence and the mentioned optimized conditions, the subsequent γ-ray analysis steps involved E_γ projections, E_γ-E_γ matrices, and an E_γ-E_γ-E_γ cube. These objects were inspected by means of the Radware software package [43] and the spectrum-analysis code TV [44]. E_γ projections and E_γ-E_γ matrices required always a coincidence with at least one of the selective transitions mentioned above. The inspection of the E_γ-E_γ-E_γ cube engaged always one or more of these transitions as well. The analysis resulted in the experimental high-spin level scheme of ^{63}Ga shown in Fig. 1.

The selectivity for ^{63}Ga can be judged by the γ-ray spectra displayed in Fig. 2 and Fig. 3 described in detail in Sec. IV.

Rotational bands in the $A \approx 60$ region are known to have γ-ray transition energies in the range $E_\gamma \approx [1.5, 4.0]$ MeV. Usually, these γ rays are emitted while the nucleus is still inside the thin target layer, i.e., while moving with slightly higher velocities than used for standard Doppler corrections adopted for γ-ray transitions in the lower part of the level scheme. These γ rays are typically emitted after the recoiling nuclei left the target. For the present analysis of ^{63}Ga and in

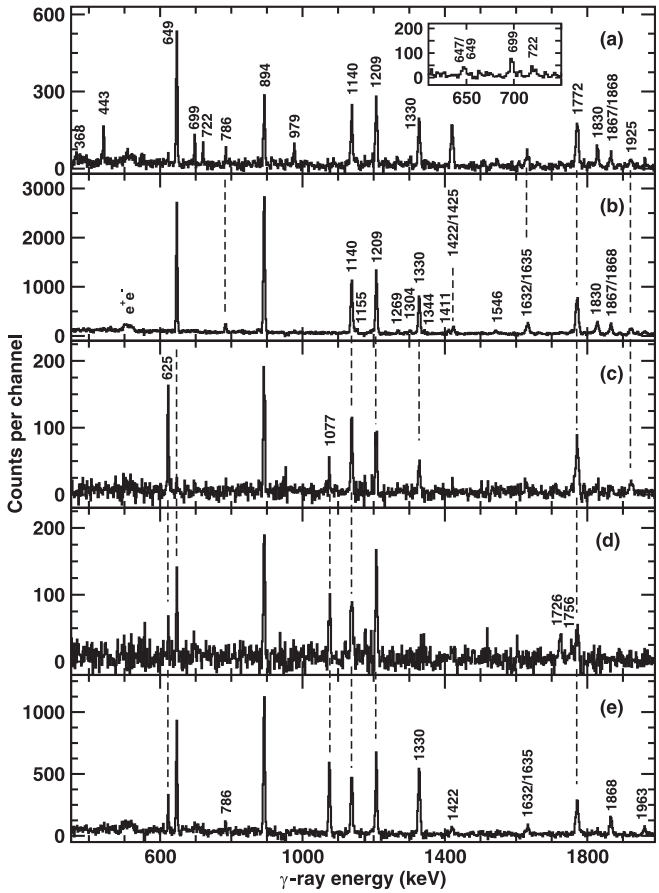

FIG. 2. Gamma-ray spectra related to the main yrast structure of ^{63}Ga shown in Fig. 1. All spectra are subject to the preselection for the analysis of ^{63}Ga residues outlined in Sec. III. Panel (a) is the spectrum taken in coincidence with the 625-keV transition and any of the two 894- or 1140-keV transitions. The inset is part of a spectrum in coincidence with the 625- and 649-keV transitions. Panel (b) is the spectrum taken in coincidence with the 1077-keV transition and any of the two 894- or 1140-keV transitions. Panel (c) is the spectrum taken in coincidence with the 649-keV transition and the 1422-/1425-keV doublet. Panel (d) is the spectrum taken in coincidence with the 1546-keV transition and any of the three 649-, 894-, or 1140-keV transitions. Panel (e) is the spectrum taken in coincidence with the 1830-keV transition and any of the five 625-, 649-, 894-, 1140-keV, or 1772-keV transitions. The binning is 2 keV per channel. Energy labels are in keV. Dashed vertical lines are meant to guide the eye.

view of the previously reported level scheme in Fig. 1 [30], a corresponding "$F\tau$-correction" was implemented for the range $E_\gamma = [1.5, 3.5]$ MeV. A more comprehensive description of how this Doppler-shift correction method was applied to the data set can be found in, for instance, Refs. [13,38].

Spins and parities assigned to the excited levels were based on the analysis of directional E_γ-E_γ correlations of oriented states (DCO ratios). For this analysis, and in line with previous studies (see, e.g., Refs. [12–16]) the Ge detectors of Gammasphere were grouped into two "pseudo rings" named "30" and "83." Two DCO matrices were studied, namely one with and one without, the ^{63}Ga-selective γ-ray coincidences mentioned earlier. The γ rays for the reaction-channel selection could be detected in any detector at any angle of the Gammasphere spectrometer. The remaining γ rays detected at 30° were sorted on one axis and those detected at 83° placed on the other axis of the DCO matrix.

DCO ratios were then derived according to

$$R_{\mathrm{DCO}}(30\text{-}83) = \frac{I(\gamma_1 \text{ at } 30^\circ; \text{gated with } \gamma_2 \text{ at } 83^\circ)}{I(\gamma_1 \text{ at } 83^\circ; \text{gated with } \gamma_2 \text{ at } 30^\circ)}.$$

Known stretched $E2$ transitions, i.e., $I \to I-2$ transitions, were used for gating. In this case one expects $R_{\mathrm{DCO}}(30\text{-}83) = 1.0$ for observed stretched $E2$ transitions and $R_{\mathrm{DCO}}(30\text{-}83) \approx 0.6$ for stretched pure $\Delta I = 1$ transitions. Deviations from the estimates for pure $\Delta I = 1$ transitions indicate a nonzero mixing ratio of the respective transition, namely $\delta(E2/M1) > 0 (< 0)$ for numbers smaller (larger) than expected for $R_{\mathrm{DCO}}(30\text{-}83)$. Nonstretched $\Delta I = 0$ transitions yield typically $R_{\mathrm{DCO}}(30\text{-}83) \approx 0.9$, i.e., numbers similar to stretched $E2$ transitions. Note, however, that since the γ-ray decay paths in nuclei populated via fusion-evaporation reactions follow the yrast line, $\Delta I = 0$ transitions are not common and usually have small relative intensities.

IV. EXPERIMENTAL RESULTS

Figure 1 shows the level scheme of ^{63}Ga deduced from the present study. The yrast structure up to the 10 870-keV $35/2^{(-)}$ (labeled gb, B1, and B2 in Fig. 1) and 12 738-keV $37/2^{(-)}$ (B3) levels is consistent with the work by Weiszflog *et al.* [30]. The 1963-1632-keV connection from B2 toward the 14 465-keV 41/2 state B4 is also confirmed, while γ rays assigned to other side structures reported in Ref. [30] were ordered somewhat differently into bands B4 and B5 in Fig. 1, owing to superior statistics of the present data set. The nine rotational bands (Q1–Q9) in Fig. 1 have not been observed previously.

At this point we like to note that parts of the ^{63}Ga level scheme posed challenges. This is primarily due to a number of known and new doublet structures in the yrast region of the level scheme; for instance, the 894.3-893.9-keV $13/2^+ \to 9/2^+ \to 9/2^-$ sequence (B1) [29], the 1422-keV $7/2^- \to 3/2^-$ (gb), and 1425-keV $33/2 \to 29/2$ (B4) transitions, the 1635-keV $21/2^+ \to 17/2^+$ (B1) and 1632-keV $41/2 \to 37/2$ (B4) transitions, the 1772-keV $19/2^{(-)} \to 17/2^+$ (B2-B1) and 1773-keV $29/2 \to 27/2^{(-)}$ (B4-B2) transitions, or the 1867-keV $33/2 \to 31/2^{(-)}$ (B4-B2) and 1868-keV $37/2^{(-)} \to 35/2^{(-)}$ (B3-B2) transitions, to name but a few. While there were typically ample options and sufficient statistics to settle the $\gamma\gamma\gamma$-coincidence relationships, the extraction of reliable DCO ratios, and thus more definite spin-parity assignments to the excited states, was hampered by these highly interconnected, and often similarly intense, γ-ray doublets. Occasionally it was also difficult to suppress remaining ambiguities from transitions belonging to ^{62}Zn [16] (see Sec. III).

The numerical results of the present study are summarized in Table I. This includes energies and spin-parity assignments of the levels placed in the decay scheme of Fig. 1 and the energies, relative intensities, DCO ratios, and multipole assignments of the γ-ray transitions. The intensities are

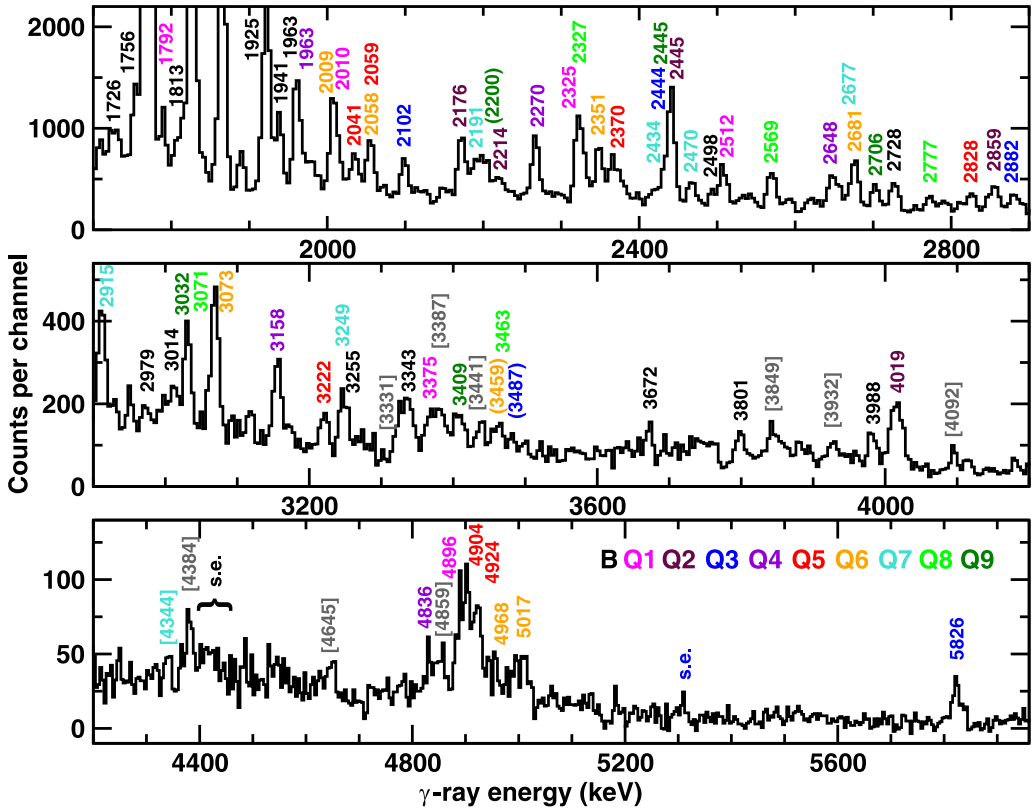

FIG. 3. Gamma-ray reference spectrum for the newly observed high-spin part of the level scheme of ^{63}Ga. The spectrum is in coincidence with either the 649- or 894-keV transitions, which serve as additional selection of ^{63}Ga residues, and any of the other intense transitions found to belong to ^{63}Ga, namely those at 75, 625, 649, 894, 1077, 1140, 1209, 1330, 1422/1425, 1632/1635, 1772/1773, 1830, 1867/1868, 1925, 1941, and 1963 keV. The binning is 4 keV per channel. Energy labels are in keV. In case the labels are given in parentheses, the transitions are tentatively placed in the level scheme in Fig. 1. In case the labels are given in brackets (mostly gray), the transitions could not be unambiguously placed into the level scheme in Fig. 1, though they are likely to directly connect into one of the states at 10 870, 10 908, 10 962, 12 738, or 12 833 keV. The color code of the labels refers to the band structures introduced in connection with Fig. 1. The note "s.e." stands for "single escape."

normalized to the 894.3 keV $13/2^+ \rightarrow 9/2^+$ transition and generally have an associated 3% systematic uncertainty from the efficiency calibration.

1. The low-spin region (gb) and band B1

Figure 2 shows five γ-ray spectra which focus on the minor revisions and additions of the previously reported part of the level scheme [29,30,37]. Figure 2(a) is the spectrum taken in coincidence with the 625-keV $9/2^+ \rightarrow 7/2^-$ transition and one of the 894- or 1140-keV transitions forming the yrast $17/2^+ \rightarrow 13/2^+ \rightarrow 9/2^+$ sequence. Besides the peaks of the γ rays forming the near-yrast structures toward higher spins, lines at 368, 443, 699, 722, and 979 keV can be seen. They confirm the 443-979- and 722-699-keV sequences [30] parallel to the originally reported 1422-keV transition [29]. In combination with yrast arguments, the DCO ratios of the 443- and 979-keV transitions led to a tentative $3/2^-$ assignment of the state at 443 keV. Its position in the level scheme could be fixed by the observation of the weak 368-keV transition, which connects to the yrast $5/2^-$ state at 75 keV, as proposed in Ref. [37] as well. The inset of Fig. 2(a) shows the relevant fraction of a spectrum in coincidence with the 625-keV line and the intense 649-keV $23/2^{(-)} \rightarrow 19/2^{(-)}$ transition. This transition was thus found to comprise a small self-coincident component, which led to the addition of a weak 647-keV transition connecting the level at 722 keV with the yrast $5/2^-$ state at 75 keV. A weak transition of that energy was also observed in Ref. [37] but not placed into their level scheme.

A level at 872 keV was introduced in Ref. [37], decaying in parallel via a 872-keV transition into the $3/2^-$ ground state and a 796-keV transition into the 75-keV $5/2^-$ state. In our high-spin data we do observe a weak 796-keV γ ray in coincidence with the 75-keV $5/2^- \rightarrow 3/2^-$ transition, consistent with the findings in Ref. [37]. However, this coincidence is very weak and no further information can be obtained as to the continuation beyond the 872-keV state. This is indicative for a low-spin side structure in ^{63}Ga. We are not sensitive to the weak 2046-keV $9/2^+ \rightarrow 3/2^-$ branch suggested in Ref. [37] because of several, more intense transitions of similar energy in the high-spin part of the ^{63}Ga level scheme (see below).

To search for an anticipated 1347-keV $7/2^- \rightarrow 5/2^-$ yrast transition, spectra in coincidence with the 625-keV line and the 1209- or 1330-keV transitions higher up in the yrast scheme were inspected. Note that the latter transitions are parallel to the 1344-keV $29/2^{(-)} \rightarrow 25/2^{(-)}$

TABLE I. Energy levels in ^{63}Ga, the transition energies and relative intensities of the γ rays placed in the level scheme, their DCO ratios and multipole assignments, and the derived spins and parities of the initial and final states of the γ rays.

E_x (keV)	E_γ (keV)	$I_{\rm rel}$ (%)[a]	Gate[b]	$R_{\rm DCO}30^\circ$–83°	Mult. Ass.	$I_i^\pi(\hbar)$	$I_f^\pi(\hbar)$
75.3(2)	75.4(3)	715[c]			$M1$[d]	$5/2^-$	$3/2^-$
443.3(2)	368.0(4)	7(2)	A	$\ll 1$	$(E2/M1)$	$(3/2^-)$	$5/2^-$
	443.3(2)	36(4)	A	0.94(19)	$(\Delta I=0)$	$(3/2^-)$	$3/2^-$
722.3(2)	279.2(4)	2(1)			$(E2/M1)$	$(5/2^-)$	$(3/2^-)$
	647.1(5)	20(7)		[e]	$(\Delta I=0)$	$(5/2^-)$	$5/2^-$
	722.2(3)	29(4)			$(\Delta I=1)$	$(5/2^-)$	$3/2^-$
1152.5(4)	1077.2(5)	833(27)	B	0.99(6)	$E2$[d]	$9/2^-$	$5/2^-$
1421.7(3)	699.3(3)	42(3)	A	1.34(35)	$(E2/M1)$	$7/2^-$	$(5/2^-)$
	978.6(4)	38(2)	A	1.10(31)	$(E2)$	$7/2^-$	$(3/2^-)$
	1421.6(6)	141(5)	A	1.00(8)[e]	$E2$	$7/2^-$	$3/2^-$
2046.4(4)	624.7(3)	205(8)	A	0.71(6)	$E1$[d]	$9/2^+$	$7/2^-$
	893.9(5)	817(27)	B	0.99(5)[e]	$\Delta I=0$[d]	$9/2^+$	$9/2^-$
2940.7(5)	894.3(4)	1000(32)	B	0.99(5)[e]	$E2$[d]	$13/2^+$	$9/2^+$
4080.5(8)	1139.8(4)	899(29)	C	1.02(5)	$E2$	$17/2^+$	$13/2^+$
5244.4(9)	2304.2(16)	11(4)					$13/2^+$
5715.8(8)	1635.4(8)	105(5)	B	1.16(13)[e]	$E2$	$21/2^+$	$17/2^+$
5853.0(8)	608.6(6)	8(2)				$19/2^{(-)}$	
	1772.2(7)	766(27)	C	0.54(3)	$(E)1$[f]	$19/2^{(-)}$	$17/2^+$
6501.6(8)	648.6(2)	759(26)	B	1.00(6)	$E2$	$23/2^{(-)}$	$19/2^{(-)}$
	785.8(3)	74(5)	C	0.73(9)	$(E)1$[f]	$23/2^{(-)}$	$21/2^+$
7335.2(11)	3255.1(22)	8(1)			$\Delta I=2$	21/2	$17/2^+$
7656.9(10)	1155.2(6)	37(3)	C	≈ 1	$(\Delta I=0)$	(23/2)	$23/2^{(-)}$
	1804.0(11)	17(3)			$(E2)$	(23/2)	$19/2^{(-)}$
7710.6(9)	1209.1(4)	687(23)	C	1.08(6)	$E2$	$27/2^{(-)}$	$23/2^{(-)}$
7912.1(10)	1410.6(6)	34(3)	C	0.36(8)	$E2/M1$	$25/2^{(-)}$	$23/2^{(-)}$
8214.0(10)	878.9(6)	17(2)			$\Delta I=2$	25/2	21/2
	1712.4(8)	8(2)			$\Delta I=1$	25/2	$23/2^{(-)}$
	2497.9(12)	26(3)			$\Delta I=2$	25/2	$21/2^+$
8857.3(10)	1146.8(8)	38(3)	C	≈ 1[e]	$(\Delta I=0)$	(27/2)	$27/2^{(-)}$
	1200.2(8)	28(3)	C	≈ 1	$(E2)$	(27/2)	(23/2)
9040.4(10)	1329.6(5)	482(17)	C	1.14(7)	$E2$	$31/2^{(-)}$	$27/2^{(-)}$
9256.1(10)	1344.0(8)	22(2)			$E2$	$29/2^{(-)}$	$25/2^{(-)}$
	1545.6(7)	53(3)	C	0.31(6)	$E2/M1$	$29/2^{(-)}$	$27/2^{(-)}$
9483.3(10)	1269.2(6)	41(3)	D	0.94(17)	$E2$	29/2	25/2
	1773.0(10)	54(7)	E	0.62(8)[e]	$\Delta I=1$	29/2	$27/2^{(-)}$
10161.5(14)[g]	1304.2(10)	21(2)	C	1.02(23)	$(E2)$	(31/2)	(27/2)
10870.1(11)	1829.8(8)	210(9)	F	1.02(7)	$E2$	$35/2^{(-)}$	$31/2^{(-)}$
10908.1(11)	1424.9(7)	47(4)	C	1.06(8)[e]	$E2$	33/2	29/2
	1867.3(9)	75(4)	F	0.35(3)[e]	$\Delta I=1$	33/2	$31/2^{(-)}$
10982.0(11)	1726.3(9)	40(3)	C	1.06(16)	$E2$	$33/2^{(-)}$	$29/2^{(-)}$
	1941.2(9)	59(4)	F	0.25(8)	$E2/M1$	$33/2^{(-)}$	$31/2^{(-)}$
11974.2(18)	1812.7(10)	17(3)					(31/2)
12738.3(12)	1756.4(8)	55(4)	C	1.15(17)	$E2$	$37/2^{(-)}$	$33/2^{(-)}$
	1868.2(9)	77(4)	G	0.27(3)	$E2/M1$	$37/2^{(-)}$	$35/2^{(-)}$
12833.1(12)	1924.8(9)	96(5)	H	0.95(7)	$E2$	37/2	33/2
	1963.4(10)	18(2)	I	0.84(17)[e]	$\Delta I=1$	37/2	$35/2^{(-)}$
14213.7(21)	3343.4(22)	13(1)			$\Delta I=2$	39/2	$35/2^{(-)}$
14465.0(14)	1631.9(8)	69(4)	J	0.95(7)	$E2$	41/2	37/2
14542.3(26)	3671.9(31)	7(1)			$(E2)$[h]	(39/2)	$35/2^{(-)}$
16634.4(28)	3801.3(25)	8(1)					37/2
17172.0(24)	2707.0(19)	8(2)					41/2
17193.3(20)	2728.4(17)	19(2)	J	0.63(19)	$\Delta I=1$	43/2	41/2
	2979.3(22)	4(2)			$\Delta I=2$	43/2	39/2
17479.1(23)	3014.1(18)	10(2)					41/2
18452.9(31)	3987.9(27)	6(1)					41/2
19034.2(33)	2399.8(18)	5(1)					

TABLE I. (*Continued.*)

E_x (keV)	E_γ (keV)	$I_{\rm rel}$ (%)[a]	Gate[b]	$R_{\rm DCO}30^\circ$-83°	Mult. Ass.	$I_i^\pi(\hbar)$	$I_f^\pi(\hbar)$
Q1							
15766.0(40)	4895.9(38)	9(1)	J	1.05(18)[e]	$(E2)$	$(39/2^-)$	$35/2^{(-)}$
18090.6(42)	1662.3(11)	7(1)			$(E2)$[h]	$(43/2^-)$	$(39/2^-)$
	1792.1(11)	17(2)	J	1.05(16)	$(E2)$	$(43/2^-)$	$(39/2^-)$
	2324.6(13)	23(2)	J	1.21(15)	$(E2)$	$(43/2^-)$	$(39/2^-)$
20101.0(44)	2010.4(13)	42(3)	J	1.12(14)	$(E2)$	$(47/2^-)$	$(43/2^-)$
22613.0(47)	2512.0(16)	21(2)	J	1.19(16)	$(E2)$	$(51/2^-)$	$(47/2^-)$
25987.6(55)	3374.6(29)	5(1)			$(E2)$[h]	$(55/2^-)$	$(51/2^-)$
Q2							
16756.6(25)	2214.2(20)	6(1)			$(\Delta I=1)$	$(41/2^-)$	$(39/2)$
	4018.5(28)	25(2)	J	1.17(24)	$(E2)$	$(41/2^-)$	$37/2^{(-)}$
18932.7(28)	2176.1(13)	27(2)	J	1.13(16)	$(E2)$	$(45/2^-)$	$(41/2^-)$
21377.4(33)	2444.8(17)	22(2)	J	1.04(12)[e]	$(E2)$[h]	$(49/2^-)$	$(45/2^-)$
24236.1(38)	2858.6(19)	13(2)			$(E2)$[h]	$(53/2^-)$	$(49/2^-)$
Q3							
16695.7(57)	1555.1(13)	10(2)			$(E2)$[h]	$(39/2^-)$	$(35/2^-)$
	5825.6(56)	6(1)	J	0.90(37)	$(E2)$[h]	$(39/2^-)$	$35/2^{(-)}$
18524.5(58)	1828.8(12)	24(3)		[e]	$(E2)$[h]	$(43/2^-)$	$(39/2^-)$
20626.1(60)	2101.6(13)	24(3)	J	1.11(20)	$(E2)$	$(47/2^-)$	$(43/2^-)$
23070.3(62)	2444.2(15)	17(2)	J	1.04(12)[e]	$(E2)$[h]	$(51/2^-)$	$(47/2^-)$
25952.9(64)	2882.6(18)	13(3)			$(E2)$[h]	$(55/2^-)$	$(51/2^-)$
29439.7(69)	3486.8(26)	4(1)			$(E2)$[h]	$(59/2^-)$	$(55/2^-)$
Q4							
17574.7(44)	4836.4(42)	7(1)			$(E2)$[h]	$(41/2^-)$	$37/2^{(-)}$
19537.4(46)	1962.7(13)	26(2)	I	0.84(17)[e]	$(E2)$[h]	$(45/2-)$	$(41/2^-)$
21807.0(48)	2269.6(14)	33(2)	J	1.02(19)	$(E2)$	$(49/2-)$	$(45/2^-)$
24455.3(50)	2648.3(15)	25(2)	J	1.26(21)	$(E2)$	$(53/2-)$	$(49/2^-)$
27613.4(53)	3158.1(19)	12(1)			$(E2)$[h]	$(57/2^-)$	$(53/2^-)$
Q5							
17643.0(32)	4903.7(41)	7(1)	J	1.05(18)[e]	$(E2)$	$(41/2^-)$	$37/2^{(-)}$
17661.4(32)	4924.1(40)	10(1)	J	1.05(18)[e]	$(E2)$	$(41/2^-)$	$37/2^{(-)}$
19702.4(32)	2041.1(12)	13(2)			$(E2)$[h]	$(45/2^-)$	$(41/2^-)$
	2059.4(13)	11(2)	J	1.07(18)[e]	$(E2)$	$(45/2^-)$	$(41/2^-)$
22072.9(35)	2370.4(13)	23(2)	J	1.18(21)	$(E2)$	$(49/2^-)$	$(45/2^-)$
24901.2(39)	2828.3(17)	16(2)			$(E2)$[h]	$(53/2^-)$	$(49/2^-)$
28123.4(44)	3222.3(21)	6(1)			$(E2)$[h]	$(57/2^-)$	$(53/2^-)$
Q6							
17706.4(40)	4968.3(51)	4(1)	J	1.11(26)[e]	$(E2)$	$(41/2^-)$	$37/2^{(-)}$
17755.4(40)	5016.9(55)	7(1)	J	1.11(26)[e]	$(E2)$	$(41/2^-)$	$37/2^{(-)}$
19764.8(40)	2009.3(14)	7(2)	J	1.12(14)[e]	$(E2)$	$(45/2^-)$	$(41/2^-)$
	2058.4(13)	5(2)	J	1.07(18)[e]	$(E2)$	$(45/2^-)$	$(41/2^-)$
22115.4(42)	2350.7(13)	12(2)			$(E2)$[h]	$(49/2^-)$	$(45/2^-)$
24796.8(45)	2681.3(16)	11(2)	J	1.18(17)[e]	$(E2)$	$(53/2^-)$	$(49/2^-)$
27869.7(51)	3072.9(23)	7(1)		[e]	$(E2)$[h]	$(57/2^-)$	$(53/2^-)$
31328.7(58)	3459.0(29)	2(1)		[e]	$(E2)$[h]	$(61/2^-)$	$(57/2^-)$
Q7							
21191.2(13)[i]	2191.2(13)	11(1)		[e]	$(E2)$[h]	(I_1+2)	I_1
23661.6(19)	2433.8(15)	7(1)				(I_1+4)	
	2470.4(14)	18(2)			$(E2)$[h]	(I_1+4)	(I_1+2)
26339.0(25)	2677.4(16)	26(2)	J	1.18(17)[e]	$(E2)$	(I_1+6)	(I_1+4)
29254.0(30)	2915.0(17)	21(2)	J	1.18(27)	$(E2)$	(I_1+8)	(I_1+6)
32502.6(37)	3248.6(22)	12(2)			$(E2)$[h]	(I_1+10)	(I_1+8)
Q8							
22627.0(14)[i]	2327.0(14)	11(1)		[e]	$(E2)$[h]	(I_2+2)	I_2
25196.2(21)	2569.2(15)	22(2)	J	1.01(19)	$(E2)$	(I_2+4)	(I_2+2)
27972.8(26)	2776.6(16)	17(2)	J	1.01(22)	$(E2)$	(I_2+6)	(I_2+4)
31043.4(33)	3070.6(20)	13(2)		[e]	$(E2)$[h]	(I_2+8)	(I_2+6)
34506.4(41)	3463.0(24)	4(1)		[e]	$(E2)$[h]	(I_2+10)	(I_2+8)

TABLE I. (*Continued.*)

E_x (keV)	E_γ (keV)	I_{rel}[a] (%)	Gate[b]	R_{DCO} 30°-83°	Mult. Ass.	I_i^π ($\hbar$)	I_f^π ($\hbar$)
Q9							
21400.0(19)[i]	2200.0(19)	8(1)		[e]	$(E2)$[h]	(I_3+2)	I_3
23844.9(25)	2444.9(16)	20(2)	J	1.04(12)[e]	$(E2)$[h]	(I_3+4)	(I_3+2)
26550.4(30)	2705.5(17)	19(2)		[e]	$(E2)$[h]	(I_3+6)	(I_3+4)
29582.2(37)	3031.8(21)	19(2)	J	1.22(25)	$(E2)$	(I_3+8)	(I_3+6)
32991.5(43)	3409.3(23)	13(2)			$(E2)$[h]	(I_3+10)	(I_3+8)

[a]Relative intensities have an associated 3% systematic uncertainty from the efficiency calibration.
[b]A: 894 and 1140 keV; B: 1140 keV; C: 649 and 1140 keV; D: 1425 keV and C; E: 1425 keV; F: 1209 and 1330 keV and C; G: 1830 keV; H: 1425 keV and F; I: 1830 keV and F; J: 649, 1209, 1330, 1425, 1632, 1830, and 1925 keV.
[c]Intensity set to match feeding 1077-keV transition. Sequence and spin-parity assignment taken from earlier work [29,30,35].
[d]Multipolarities and spin-parity assignments taken from earlier work [29,30,35].
[e]Doublet structure—individual DCO ratios are difficult or sometimes impossible to extract.
[f]The notation "(E)1" indicates that the multipole order of the transition is dipole ($\Delta I = 1$), while there is tentative evidence pointing toward an electric dipole ($E1$) rather than magnetic dipole ($M1$) assignment. See text for discussion.
[g]Tentative level energy. Populating och depopulating γ-ray transitions can be subject to exchange.
[h]Tentative multipolarity assignments based on rotational character and yrast arguments.
[i]Calculated from $X_1 = 19\,000$, $X_2 = 20\,300$, and $X_3 = 19\,200$ keV.

transition. The search for this 1347-keV transition proved negative (cf. Sec. V A). Finally, the DCO ratios determined for the main transitions in this low-lying part of the level scheme confirmed the previous γ-ray multipolarity and derived spin-parity assignments up to the 4081-keV $17/2^+$ state [29,30,34–37].

2. The medium-spin region: Bands B2–B5

The spectrum in Fig. 2(b) is in coincidence with the low-lying 1077-keV $9/2^- \rightarrow 5/2^-$ yrast transition and either one of the 894- or 1140-keV yrast transitions placed on top of it. Hence, this spectrum can be considered a reference spectrum for the near yrast structures up to the 10 870-, 11 974-, 12 738-, and 14 465-keV states, respectively, They are labeled B2–B5 in Fig. 1. Cascade B2 is formed by the established [30] 1830-1330-1209-649-keV $E2$ sequence, connecting via the 1772-keV dipole transition into the yrast 4081-keV $17/2^+$ state (B1). The DCO ratio of the 1772-keV is slightly below 0.6, which is indicative of a small quadrupole admixture. However, since there is the 1773-keV doublet (see below) and because $g_{9/2} \rightarrow f_{5/2}$ $M2$ decay strength cannot be ruled out in this mass region, the parity of B2 (and all further dependencies) was assigned only tentatively, in line with a similar decision taken in Ref. [30]. The parallel 786-1635- and, rather weak, 609-2304-keV cascades were confirmed as well. At variance, weak transitions at 1147, 1155, 1200, 1304, and 1813 keV were grouped into one sequence (B5) rather than the two in Ref. [30].

The spectrum in Fig. 2(c) aims at structure B4. It is in coincidence with the 649-keV $23/2^{(-)} \rightarrow 19/2^{(-)}$ yrast transition and the 1422-keV $7/2^- \rightarrow 3/2^-$ (gb) and 1425-keV $33/2 \rightarrow 29/2$ (B4) doublet. In this spectrum, the efficiency-corrected yield of the 1772 keV transition was found to be about twice that of the 1209-keV transition. In combination with coincidence and sum-energy relations of the other transitions in, and in between, cascades B2 and B4, Fig. 2(c) led to the placement of the 1773-keV transition between 9483- and 7711-keV states. The coincidence relations within band B4 were found consistent with those proposed previously [30], with the exception of the 879-keV transition, which was moved into that structure as well. The key transition is the one newly observed at 3255 keV, as $3255 + 879 \approx 1635 + 2498$. The sequence of the 3255- and 879-keV transitions is based on yrast arguments. Missing yield in the decay of the 7335-keV level can be explained by very weak and hence unresolved transitions into, for instance, the 6502- or 5853-keV states. A 1292-keV line reported coincident with the 879-keV transition in Ref. [30] was observed, but could not be placed firmly into the level scheme of Fig. 1. The DCO ratios of the 1773-, 1867-, and 1963-keV transitions, though all doublets, point toward stretched $\Delta I = 1$ character. That assignment implies a spin difference of four units of angular momentum between the 8214-keV $25/2$ and the 4081-keV $17/2^+$ levels. Consequently, positive-parity of band B4 is highly favored. Nevertheless, due to ambiguities in the DCO ratios we refrain from an explicit assignment.

The spectrum in Fig. 2(d) is focused on structure B3, which besides some adjustments of γ-ray energies was found to agree with previous work [30]. The coincidence requirement with the 1546-keV $29/2^{(-)} \rightarrow 27/2^{(-)}$ transition highlights the 1726- to 1756-keV $E2$ cascade toward higher spin states within B3. Notably, the DCO ratios of all four transition connecting B3 with B2 have rather low values, $R_{DCO} \approx 0.30$ (cf. Table I). This implies stretched dipole character with considerable quadrupole admixture, i.e., $E2/M1$ transitions with $\delta(E2/M1) > 1$. Thus, the parities of the states in B2 and B3 must be the same. Figure 2(e) is a spectrum in coincidence with the 1830-keV $35/2^{(-)} \rightarrow 31/2^{(-)}$ transition and several other intense transitions from B2 or B1. This spectrum proves the presence of the 1868-keV doublet transition into band B3 as well as the 1963-keV connection toward B4 and the 1632-keV transition on its top. The respective state at

$E_x = 14465$ keV and $I = 41/2$ was the highest one reported in Ref. [30].

3. The high-spin region: Quadrupole bands Q1–Q9

The spectrum in Fig. 3 is considered the reference spectrum for the newly observed high-spin part of the level scheme of ^{63}Ga, namely the well-deformed band structures labeled Q1–Q9. The spectrum is in coincidence with either the 649- or 894-keV transitions, which serve as additional selection of ^{63}Ga residues, and any of the other reasonably intense transitions found to belong to ^{63}Ga, namely those at 75, 625, 649, 894, 1077, 1140, 1209, 1330, 1422/1425, 1632/1635, 1772/1773, 1830, 1867/1868, 1925, 1941, and 1963 keV. Note, in Fig. 3 the top of the peaks at 1772/1773, 1830, and 1867/1868 keV are off scale. In turn, a plethora of peaks at high energy could be resolved, with relative intensities on the order of $I_{\rm rel} \approx 0.5\,\%$ to $5\,\%$ (cf. Table I). A few of the high-energy transitions observed in Fig. 3 could be connected to high-lying states of band B4, see right-hand side of Fig. 1. Here, the DCO ratio of the 2728-keV transition provided the spin assignment of the 17 193-keV level and, indirectly, the one of the 14 214-keV state. The vast majority of the remaining lines, however, could be grouped into nine rotational bands. In-band transitions were primarily observed in the γ-energy range between 1.8 and 3.5 MeV, while a number of transitions linking the bands directly to the known part of the level scheme were identified between 4- and 6-MeV γ-ray energy. Noteworthy in Fig. 3 are the topmost 5826-keV transition and the "bump" of several transitions around 4.9 MeV, as well as its corresponding single-escape structure 511 keV lower in energy.

In the following, bands Q1–Q9 are briefly described one by one in connection with the spectra displayed in Fig. 4. (In the online version, a color code is introduced for Q1–Q9, with gb and B1–B5 accounting for black or gray.) All nine spectra in Fig. 4 are subject to a coincidence with one of the following transitions established in the normally deformed part of the ^{63}Ga level scheme: 75-, 625-, 649-, 894-, 1077-, 1140-, 1209-, 1330-, 1422/1425-, or 1772/1773-keV. This selection was a compromise between maximizing statistics for the ^{63}Ga analysis while keeping disturbances from transitions of ^{62}Zn at a low, hence bearable, level. For the level scheme as displayed in Fig. 1, of course, many more spectra were thoroughly prepared and inspected for each of the bands.

In addition to the base requirements outlined above, the spectrum in Fig. 4(a) is in coincidence with either one of the 2010- or 2512-keV Q1 in-band transitions. It reveals peaks at 1662 (tentative), 1792 (intense line in ^{62}Zn as well), and 2325 keV. None of these were found to be in mutual coincidence and were thus placed next to each other at the bottom of Q1. Their summed yields nicely account for the feeding 2010-keV line (cf. Table I). Because other main transitions known to belong to ^{62}Zn [16] were *not* observed in spectra related to the analysis of Q1, the 1792-keV line was assigned to Q1 in ^{63}Ga. In addition, a weak peak at 4896 keV was observed in

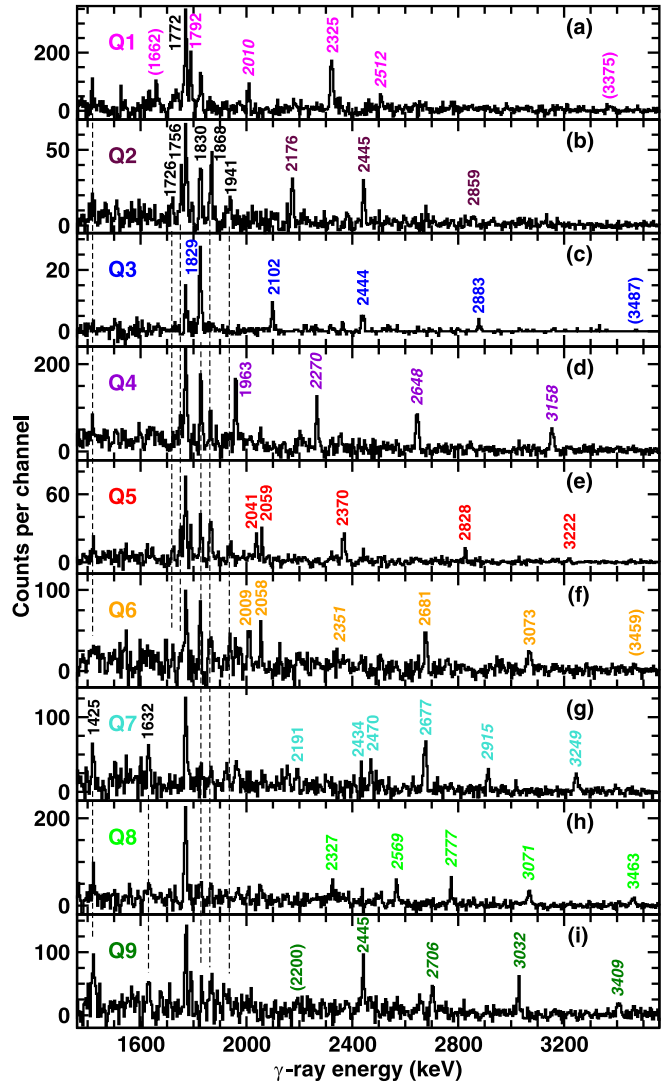

FIG. 4. Gamma-ray spectra illustrating the nine high-spin rotational bands Q1 through Q9 in panels (a) through (i). The binning is 4 keV per channel. Energy labels are in keV. In case the labels are given in parentheses, the transitions are tentatively placed in the level scheme in Fig. 1. The color code of the labels refers to the band structures introduced in connection with Fig. 1. All spectra are subject to the pre-selection for the analysis of ^{63}Ga residues outlined in Sec. III and are in coincidence with any of the 75-, 625-, 649-, 894-, 1077-, 1140-, 1209-, 1330-, 1422/1425-, or 1772/1773-keV transitions. In addition, panel (a) is in coincidence with the 2010- and 2512-keV transitions. Panel (b) is in coincidence with the 4019-keV transition. Panel (c) is taken in coincidence with the 5826-keV transition. Panel (d) is in coincidence with the 2270-, 2648-, or 3158-keV transitions. Panel (e) is in coincidence with the 4904- or 4924-keV transitions. Panel (f) is in coincidence with the 2351-keV transition. Panel (g) is in coincidence with the 2915 or 3249-keV transitions. Panel (h) is in coincidence with the 2569-, 2777-, or 3071-keV transitions. Panel (i) is in coincidence with the 2706-, 3032-, or 3409-keV transitions. These coincidence requirements are also indicated by a slanted energy label in the respective panel. Dashed vertical lines are meant to guide the eye.

coincidence with the 2010-, 2512-, and 2325-keV transitions. The spectrum Fig. 4(a) lacks peaks at, for instance, 1632, 1756, 1867, or 1925 keV. Thus, Q1 is directly connected to the 10 870-keV $35/2^{(-)}$ state (B2) via the 4896-keV link. In fact, a peak at 1830 keV, depopulating the 10 870-keV state, can be seen in Fig. 4(a). The assigned spin implies Q1 being very close to if not forming the yrast line, which is consistent with its rather high relative yield.

The spectrum in Fig. 4(b) is in coincidence with the 4019-keV quadrupole transition linking Q2 into the 12 738-keV $37/2^{(-)}$ state (B3). Here peaks at 1726, 1756, 1868, and 1941 keV are clearly visible, next to the 1830-keV line (B2) as well as the in-band transitions at 2176, 2445, and 2859 keV. The latter transition was confirmed by spectra in coincidence with the 2176-keV line.

The spectrum in Fig. 4(c) is in coincidence with the 5826-keV transition linking Q3 into the 10 870-keV $35/2^{(-)}$ state (B2). This state is depopulated by the 1830-keV transition, which is a doublet with the 1829-keV in-band transition, inferred from, e.g., the spectrum in Fig. 4(c): The yield of the peak at 1829/1830 keV is about twice the yield of the neighboring 1772-keV line, connecting B2 with B1. With decreasing yield, the other band members were identified at 2102, 2444, 2883, and, tentatively, 3487 keV. The latter transition was confirmed by coincidences between Q3 band members and the γ rays connecting low- to medium-spin states in ^{63}Ga (see above). In such a spectrum a weak peak at 1555 keV was observed as well, which is proposed to be an in-band member positioned underneath the 1829 keV transition.

The spectrum in Fig. 4(d) is in coincidence with one of the 2270, 2648, or 3158-keV in-band transitions of Q4. Toward lower γ-ray energies, this spectrum shows a relatively intense peak at 1963 keV, but none at 1925 keV. Thus, this γ ray was placed below the 2270-keV transition, rather than representing the 1963-keV $37/2 \rightarrow 35/2^{(-)}$ connection between B4 and B2. All four Q4 in-band transitions revealed weak, but firm, coincidences with the 4836-keV high-energy link, which due to the presence of peaks at 1726, 1756, and 1868-keV in Fig. 4(d) was assigned as connecting Q4 with the 12 738-keV $37/2^{(-)}$ state (B3).

The spectrum in Fig. 4(e) is in coincidence with the 4904- and 4924-keV quadrupole doublet. In-band transitions of Q5 were observed at 2041 and 2059 keV, which were placed in parallel as $4904 + 2059 \approx 4924 + 2041$, and at 2370, 2828, and 3222 keV. The observation of the peaks at 1726, 1756, 1868, and 1941 keV in the spectrum led us to connect Q5 with the 12 738-keV $37/2^{(-)}$ state (B3).

The findings for Q6 were very similar to Q5. In this case, the spectrum in Fig. 4(f) is in coincidence with the 2351-keV in-band transition. In the spectrum, the continuation of Q6 to higher energies and angular momenta is formed by the 2681-, 3073-, and (tentatively) 3459-keV transitions. The decay out proceeds via the parallel 2009- to 5017- and 2058- to 4968-keV cascades, both found to feed once again the 12 738-keV $37/2^{(-)}$ state (B3).

At variance with the previously discussed bands, rotational sequences Q7, Q8, and Q9 could not be connected to the main part of the level scheme of ^{63}Ga. Nevertheless, coincidence relations and coincidence yields of peaks in the lower-lying yrast sequence indicate that the γ-ray flux from these bands ends up in ^{63}Ga, but in an unresolved manner. A very weak line at 4344 keV (cf. Fig. 3) was found in several spectra inspected for Q7, but neither exit nor entry point could be unambiguously determined.

Notably, there are a few qualitative differences between the spectra in Figs. 4(g)–4(i) and Figs. 4(a)–4(f): First, transitions at 1425 and 1635 keV are enhanced, indicative of feeding into band B4 as well. Second, the main yield of the in-band transitions is shifted from ≈ 2.0 MeV to ≈ 2.4 MeV. Finally, there are many small peaks in the energy range $\approx$2.0–2.3 MeV in Figs. 4(g)–4(i), i.e., the γ-ray flux toward or in the decay-out region is more heavily fragmented for Q7, Q8, and Q9 compared with the other bands described earlier. Therefore, bands Q7, Q8, and Q9 were placed in Fig. 1 at somewhat higher excitation energies ($X_1 = 19\,000$ keV, $X_2 = 20\,300$ keV, $X_3 = 19\,200$ keV). Their placement also accounts for the option of Q8 and Q9 representing signature partner bands; $(20\,300 - 19\,200) = 2200/2$. The suggested spin values are $I_1 = I_3 = 43/2$ and $I_2 = 45/2$. In that case, these bands reach the yrast line at about 26–27 MeV excitation energy and spin $55/2$, consistent with their feeding and decay pattern illustrated in Figs. 4(g)–4(i).

V. DISCUSSION

With three valence protons and four valence neutrons outside the doubly magic $N = Z = 28$ core ^{56}Ni, the low-spin part of the level scheme of ^{63}Ga is expected to be governed by near-spherical shapes and characteristics of the interactions within the $p_{3/2}$, $p_{1/2}$, and $f_{5/2}$ orbitals, the so-called upper-fp shell. The $3/2^-$ ground state [36] and further low-lying negative-parity states (gb in Fig. 1) confirm that. However, shell-model studies of lighter odd-A Cu or Zn isotopes indicate that $f_{7/2}$ single-hole configurations can compete with configurations composed of several particles in the upper-fp orbitals [14,15]. Therefore, a shell-model assessment of the negative-parity low-lying states ($E_x < 1.5$ MeV) was conducted employing the full fp space. The details and the results are described in Sec. V A. Similar to the influence of holes in the $f_{7/2}$ shell, particles in the $\mathcal{N} = 4$ $g_{9/2}$ intruder orbitals are known to be crucial for the understanding of nuclei in the $A \approx 60$–70 region. A second set of shell-model calculations is presented in Sec. V A, using the model space $pf_{5/2}g_{9/2}$.[1]

Previous studies of ^{63}Ga [30] and many other nuclei in the $A \approx 60$-70 region clearly indicate the need to allow for excitations of one or more protons or neutrons from upper-fp orbitals into the positive-parity $g_{9/2}$ intruder orbital *and at the same time* create holes in the $f_{7/2}$ shell to describe their deformed rotational bands at high spin and high excitation energy (see, for instance, Refs. [9,13,16]). Consequently, cranked Nilsson-Strutinsky calculations were performed to investigate and classify the various medium- and high-spin bands in ^{63}Ga. That discussion is the subject of Sec. V B.

[1] A more comprehensive, full fp shell plus $g_{9/2}$, model space is to our knowledge not yet available for shell-model practitioners.

TABLE II. Comparison of experimental values and shell-model predictions of the magnetic dipole moment, μ, and the electric quadrupole moment, Q_s, of ^{63}Ga for spin $I = 3/2$ and $I = 5/2$, thereby complementing Table IV in Ref. [36].

Moment (I)	Expt. [36]	jj4b[a]	JUN45[b]	FPD6	KB3G	GXPF1A
$\mu(3/2)\,(\mu_N)$	+1.469(5)	+1.605	+1.205	+1.539	+1.463	+1.555
$Q_s(3/2)$ (eb)	+0.212(14)	+0.215	+0.239	−0.239	−0.112	+0.197
$\mu(5/2)\,(\mu_N)$	+1.652(6)	+0.909	+0.813	+1.104	+1.415	+1.311
$Q_s(5/2)$ (eb)	+0.424(25)	−0.425	−0.391	−0.272	−0.414	−0.433

[a]Calculated values taken from Ref. [36].

[b]Recalculated values; the predictions for $Q_s(I)$ differ slightly from those in Ref. [36], presumably due to use of different effective charges in Ref. [36] compared with those proposed in Ref. [32].

A. Shell-model calculations

The shell-model code ANTOINE [45,46] was used for the shell-model calculations. For calculations in the full fp space, predictions from three interactions were studied, namely FPD6 [47], GXPF1A [2], and KB3G [3]. Owing to computational limitations and the level of discussion and agreement (see below), the configuration space was truncated to allow for the excitation of up to four particles from the $1f_{7/2}$ shell into the upper fp shell, for which the notation $t = 4$ is used. The evolution of the predictions was assessed by means of preceding $t = 0$, $t = 1$, $t = 2$, and $t = 3$ calculations. To probe decay patterns on the $t = 4$ level, bare g factors were used and effective nucleon charges taken from Ref. [48], i.e., $\varepsilon_p = 1.15e$ and $\varepsilon_n = 0.80e$ for protons and neutrons, respectively. Transition strengths and deduced branching ratios and mixing ratios of the transitions and lifetimes of the nuclear states were based on the experimental γ-ray energies.

Following the association of observed and calculated levels, mean level deviations (MLD) in conjunction with binding energy shifts (BES) provide an overview of the agreement between experiment and theory in terms of energy levels. Mean branching deviations (MBD) [49] were derived to compare predicted and observed electromagnetic decay properties.

The shell-model comparison with the experimental data was complemented with unrestricted calculations in the $f_{5/2}pg_{9/2}$ space using the interaction JUN45 [32]. According to Ref. [32], $g_{s,\mathrm{eff}} = 0.7g_{s,\mathrm{free}}$ and $g_{\ell,\mathrm{eff}} = g_{\ell,\mathrm{free}}$ were used as well as the effective charges $\varepsilon_p = 1.5e$ and $\varepsilon_n = 1.1e$ for protons and neutrons, respectively. For completeness, Mizusaki and coworkers presented a brief shell-model comparison of ^{63}Ga described in Ref. [50].

Procter *et al.* validated the $3/2^-$ assignment to the ^{63}Ga ground state with shell-model predictions using the $f_{5/2}pg_{9/2}$ space (cf. Table IV in Ref. [36]). In Table II we complement that set of calculations with the predictions from the $t = 4$ calculations in the fp model space. Clearly, the predictions for the magnetic moment, $\mu(3/2)$, are in excellent agreement with the experimental number for all three interactions studied. However, only the GXPF1A interaction is in line with a positive value for the electric quadrupole moment, $Q_s(3/2)$. The predictions for $\mu(5/2)$ are somewhat larger than those from calculations in the $f_{5/2}pg_{9/2}$ space, while predictions for $Q_s(5/2)$ are of similar size and all with a negative sign. Hence, the same conclusion as Ref. [36] can be drawn, the ground state spin and parity is $3/2^-$, also supported by the calculation using the GXPF1A interaction.

1. Notes on the low-spin region

Concerning the low-lying negative parity states, up to 1.5 MeV in excitation energy, the predictions of the calculations in the fp model space are displayed in Fig. 5. The predicted decay properties are summarized in Table III, including those from the JUN45 interaction acting in the $f_{5/2}pg_{9/2}$ space. Looking at Fig. 5, there are two general observations. First, the predicted energies start converging with $t = 2$, as expected. Second, the predictions of the three interactions are remarkably different, which came as some surprise.

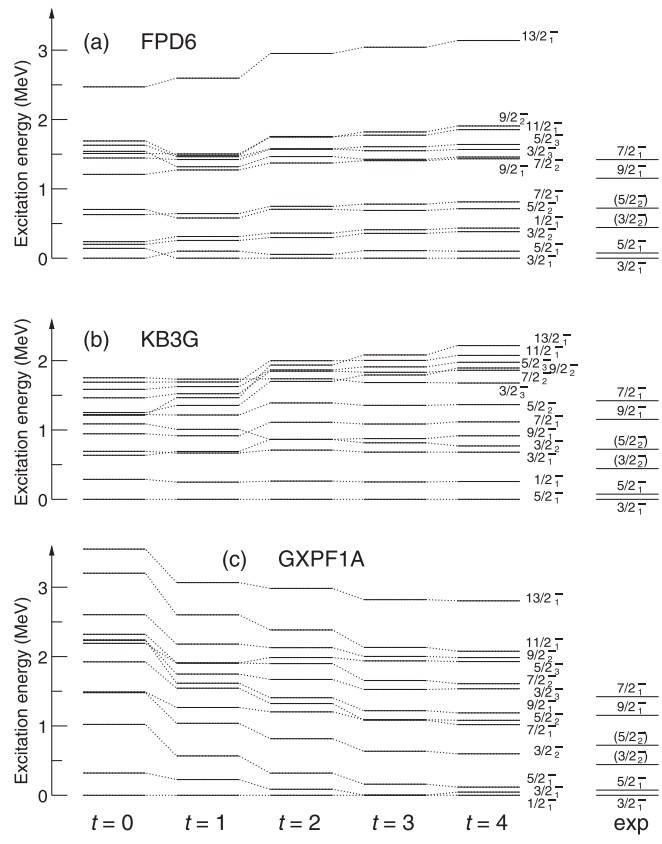

FIG. 5. Evolution of predicted low-energy negative-parity states as a function of parameter t, denoting the number of particles allowed to be excited across the shell gap at $N = Z = 28$. The different panels relate to different interactions used for the full fp shell-model space. The experimentally observed states (exp) are shown on the right-hand side of each panel. See text for details.

TABLE III. Experimental (cf. Table I and Refs. [34,35]) and predicted excitation energies, E_x, lifetimes, τ, mixing ratios, $\delta(E2/M1)$, and branching ratios, b, of low-lying negative-parity states in ^{63}Ga. Energies of unobserved levels or γ-ray transitions are listed in italic. A star, ⋆, implies use for MLD, BES, and MBD assessments. In the lower part of the Table, the possibility of assigning $7/2_1^-$ to the 1153-keV state and $7/2_2^-$ to the 1422-keV state is explored. See text for details.

E_x (keV)		I_i^π ($\hbar$)	I_f^π ($\hbar$)	E_γ (keV)	$b_{\rm exp}$	JUN45 τ (ps) b	JUN45 τ (ps) δ	FPD6 τ (ps) b	FPD6 τ (ps) δ	KB3G τ (ps) b	KB3G τ (ps) δ	GXPF1A τ (ps) b	GXPF1A τ (ps) δ
75	⋆	$5/2_1^-$				41800		1930		14600		13200	
			$3/2_1^-$	75	100	100	+0.07	100	+0.03	100	–0.05	100	+0.02
200		$1/2_1^-$				36		24		94		110	
			$5/2_1^-$	*125*	n.o.	0		0		0		0	
			$3/2_1^-$	*200*	n.o.	100	–0.05	100	–0.05	100	–0.15	100	–0.08
443	⋆	$3/2_2^-$				20		4.3		2.8		4.1	
			$1/2_1^-$	*243*	n.o.	41	+0.12	10	–0.11	0	+0.06	1	+0.48
			$5/2_1^-$	368	16(5)	25	+0.20	9	+0.35	3	+0.14	3	–0.28
			$3/2_1^-$	443	84(5)	34	+0.02	81	+0.12	97	+0.11	97	+0.05
722	⋆	$5/2_2^-$				1.1		3.7		99		3.1	
			$3/2_2^-$	279	4(2)	5	+0.07	4	+0.08	13	+1.3	2	+0.06
			$1/2_1^-$	*522*	n.o.	0		4		50		2	
			$5/2_1^-$	647	39(13)	11	+0.02	62	+0.34	33	+0.06	13	–0.12
			$3/2_1^-$	722	57(11)	84	–0.33	30	+6.4	4	–0.36	83	–0.54
1153	⋆	$9/2_1^-$				1.7		1.6		1.7		1.7	
			$5/2_2^-$	*431*	n.o.	0		0		0		0	
			$5/2_1^-$	1077	100	100		100		100		100	
1422	⋆	$7/2_1^-$				0.27		0.13		0.27		0.41	
			$9/2_1^-$	*269*	n.o.	0	+0.05	0	0.00	0	–0.02	0	+0.13
			$5/2_2^-$	699	19(2)	2	–1.2	12	–0.02	9	+0.31	3	+0.74
			$3/2_2^-$	979	17(1)	1		4		1		11	
			$5/2_1^-$	*1347*	n.o.	68	–0.86	78	+0.73	39	+6.9	69	+13
			$3/2_1^-$	1422	64(2)	29		6		51		17	
2100		$11/2_1^-$				7.0		0.53		5.9		3.9	
			$7/2_1^-$	*678*	n.o.	25		4		37		30	
			$9/2_1^-$	*947*	n.o.	75	–3.4	96	+0.34	63	+11	70	+19
3000		$13/2_1^-$				0.33		0.13		0.18		0.11	
			$11/2_1^-$	*900*	n.o.	23	+0.31	3	+0.46	1	+0.92	0	–2.0
			$9/2_1^-$	*1847*	n.o.	77		97		99		100	
MLD (keV)						149		267		330		228	
BES (keV)						–177		74		–70		–37	
MBD						0.263		0.104		0.101		0.119	
1153	⋆	$[7/2_1^-]$				0.67		0.32		0.83		1.3	
			$5/2_2^-$	*431*	n.o.	1	–0.73	7	–0.01	6	+0.19	2	+0.46
			$3/2_2^-$	*710*	n.o.	1		2		0		7	
			$5/2_1^-$	1077	100	73	–0.69	86	+0.59	39	+5.5	72	+10
			$3/2_1^-$	*1153*	n.o.	25		5		54		19	
1422	⋆	$[7/2_2^-]$				0.87		0.42		0.39		0.97	
			$7/2_1^-$	*269*	n.o.	0	+0.01	0	+0.02	0	+0.03	0	+0.29
			$5/2_2^-$	699	19(2)	1	–0.61	7	+0.03	15	–0.13	14	–0.13
			$3/2_2^-$	979	17(1)	7		0		3		17	
			$5/2_1^-$	*1347*	n.o.	68	0.00	12	–3.3	33	+0.32	3	+2.4
			$3/2_1^-$	1422	64(2)	26		80		48		66	
MLD (keV)						94		128		253		149	
BES (keV)						–258		69		–259		–121	
MBD						0.257		0.083		0.162		0.090	

Typically, for nuclei located in the $f_{7/2}$-quadrant and including neutron-deficient Ni and Cu isotopes, predictions are similar and of an excellent "spectroscopic quality" [1–3]. This allows for very intriguing studies of, for instance, isospin breaking effects in mirror nuclei [4,5]. As with the context of the $3/2^-$ ground-state spin-parity assignment, GXPF1A performs best in reproducing the observed yrast and near-yrast sequence. There is only one exception: The order of the $7/2^-_1$ and $9/2^-_1$ yrast states is interchanged. FPD6 predictions are of comparable quality. The order of the $7/2^-_1$ and $9/2^-_1$ yrast states is also an issue. The $1/2^-$ state is predicted at a considerable higher excitation energy (443 keV) compared with GXPF1A (0 keV, ground state), and the gap between the predicted $11/2^-_1$ and $13/2^-_1$ states is predicted larger than in case of GXPF1A. However, these states are yet to see an experimental counterpart. In turn, predictions from KB3G put the $7/2^-_1$ and $9/2^-_1$ yrast states into the correct order, but at too low excitation energies. At variance, KB3G predicts a $5/2^-$ ground state; the yrast $3/2^-_1$ state is placed at a high value of 680-keV excitation energy. Furthermore, the calculated gap between the $11/2^-_1$ and $13/2^-_1$ states is almost vanishing. This sequence of level of agreement is confirmed by the numbers, i.e., at first rather large and then further increasing MLD values for GXPF1A, FPD6, and KB3G predictions, respectively (cf. central rows in Table III). The best agreement for the set of low-lying states in terms of energy levels was found for the JUN45 interaction, despite its closed ^{56}Ni core.

Based on the numerical results listed in Table III, it is worth dwelling on a few more consistencies and, primarily, inconsistencies, both among the different shell-model parametrisations, but also with respect to the experimental findings. Experimentally, the 75-keV $5/2^- \rightarrow 3/2^-$ ground-state transition was established. Using this energy and the predicted $B(M1)$ and $B(E2)$ decay strength, the lifetime predictions of the 75-keV $5/2^-_1$ state range from 1.9 ns (FPD6) to 41.8 ns (JUN45). The latter is not consistent with the fact that the 75-keV transition is clearly observed in the present in-beam data, with ^{63}Ga recoils leaving the focus of the Gammasphere array at a speed of $v \approx 3\,\%\ c \approx 1$ cm/ns. All interactions predict a 100% decay branch of the hitherto unobserved $1/2^-$ yrast state into the $3/2^-$ ground state with lifetimes of several tens of picoseconds. The three calculations in the fp space provide good descriptions of the decay pattern of the yrare $3/2^-_2$ state observed at 443 keV, while JUN45 prefers a decay path via the unobserved $1/2^-_1$ state. The yrare $5/2^-_2$ state at 722 keV is, however, very well described by JUN45, likewise FPD6 and GXPF1A. Here, KB3G is off, both in terms of energy [cf. Fig. 5(b)], decay pattern, and predicted lifetime. In turn, associating the observed level at 1153 keV with the calculated $9/2^-$ yrast states, an exclusive decay branch into the 75-keV $5/2^-$ yrast state is predicted consistently as well as very similar lifetimes of that $9/2^-$ state.

None of the four interactions studied is capable of reproducing the decay pattern of the yrast $7/2^-$ state observed at 1422 keV. In fact, all four prefer a significant if not dominating mixed $E2/M1$ transition into the 75-keV $5/2^-$ yrast state, rather than the observed main $E2$ branch into the $3/2^-$ ground state. That disagreement is the major contribution to the rather large MBD values. As noted in Sec. IV, an explicit search for the respective 1347-keV $7/2^-_1 \rightarrow 5/2^-_1$ transition proved negative.

Experimentally, based on previous [29,30] and present reports, it is difficult to argue that the 894-625-1422-keV sequence does *not* comply with a quadrupole-dipole-quadrupole cascade into the ground state, i.e., $13/2^+ \rightarrow 9/2^+ \rightarrow 7/2^- \rightarrow 3/2^-$. However, one may consider the possibility to change the spin-parity assignment of the 1153-keV state from $9/2^-$ to $7/2^-$, i.e., that state representing the yrast $7/2^-_1$ and thus the 1422-keV state representing the yrare $7/2^-_2$ level. This scenario is investigated in some more detail in the lower part of Table III. Here, the 1077 keV transition would represent the $7/2^- \rightarrow 5/2^-$ dipole transition, which is predicted to have a considerable if not dominating $B(E2)$ strength, i.e., its measured angular distribution and correlation data might be similar to a stretched $\Delta I = 2$ transition. Similarly, a possibly strong $g_{9/2} \rightarrow f_{5/2}$ re-coupling can lead to a sizable $M2$ strength for the 894 keV transition connecting the 2046-keV $9/2^+_1$ state with a (in this scenario) 1153-keV $7/2^-_1$ state. Note that due to the doublet structure of this 894-keV transition, angular distribution data is not reliable and angular correlation data limited. Similar to the search for a possible 1347 keV mentioned above, the search for an 1153-keV transitions proved negative, too (cf. Table III, $[7/2^-_1] \rightarrow 3/2^-$ branch). Interestingly, for this scenario the MLD values improve for all four interactions. The overall agreement between predicted and observed decay pattern improves as well. The improvement is in fact substantial in case of FPD6 and GXPF1A, thus approaching a level of agreement usually obtained for the somewhat lighter nuclei in the $A \approx 60$ region.

As a final note on Fig. 5 and Table III, one can state that the predictions for the decay pattern of the hitherto unobserved $11/2^-$ and $13/2^-$ states are different for the different interactions studied. Interactions with isospin-breaking terms (see, e.g., Refs. [4,5]) were not considered in the present study, because the KB3G interaction in itself was found to perform comparatively poorly in the case of ^{63}Ga.

2. Notes on the medium-spin region

The parameter space of the JUN45 interaction allows a comparison with the observed structures B1, B2, B3, and B4 (cf. Fig. 1) as well. For this exercise we assign negative parity to B2 and B3 and positive parity to B4. Furthermore, for the assessment of decay patterns we assume a typical value of $B(E1) = 1 \times 10^{-5}\ e^2\,\mathrm{fm}^2$ for all parity-changing $\Delta I = 1$ transitions. Numerical results are listed in Table IV. Observed and predicted excitation energies are compared in Fig. 6. To ease related discussions within the Cranked-Nilsson Strutinsky approach, Fig. 6 provides the energies in those terms, i.e., relative to a rotating liquid drop energy [51] (see Sec. V B).

The signature partners of the structure gb were discussed earlier. Experimentally, the yrast sequence continues with the $9/2^+$-$21/2^+$-$E2$ sequence, the behavior of which is reproduced nicely by JUN45, but about 1 MeV too high in energy. This mismatch, found for several neutron-deficient Ga isotopes, was already noted and annotated in the original JUN45 publication [32]. In fact, JUN45 predicts the exper-

TABLE IV. Experimental (cf. Table I and Refs. [34,35]) and predicted excitation energies, E_x, lifetimes, τ, mixing ratios, $\delta(E2/M1)$, and branching ratios, b, of structures B2 and B3 (presumed negative parity) as well as B1 and B4 (presumed positive parity) in Fig. 1. Energies of unobserved levels or γ-ray transitions are listed in italic. A star, $\star$, implies use for MLD, BES, and MBD assessments. $E1$ strengths were set to $B(E1) = 1 \times 10^{-5}\ e^2\,\mathrm{fm}^2$ for all parity-changing $\Delta I = 1$ transitions.

E_x (keV)		I_i^π ($\hbar$)	I_f^π ($\hbar$)	E_γ (keV)	b_{exp}	JUN45 τ (ps) b	δ
B2 and B3, $\pi = -$							
5853	$\star$	$19/2^-$				11	
			$[15/2^-]$	609	1.0(3)	0	
			$17/2^+$	1772	99.0(3)	100	
6502	$\star$	$23/2^-$				16	
			$19/2^-$	649	91(1)	87	
			$21/2^+$	786	9(1)	13	
7711	$\star$	$27/2^-$				0.90	
			$23/2^-$	1209	100	100	
7912	$\star$	$25/2^-$				0.23	
			$27/2^-$	*201*	n.o.	0	+0.09
			$21/2^-$	*847*	n.o.	0	
			$23/2^-$	1411	100	100	+0.46
9040	$\star$	$31/2^-$				0.69	
			$27/2^-$	1330	100	100	
9256	$\star$	$29/2^-$				0.14	
			$31/2^-$	*216*	n.o.	0	+0.04
			$25/2^-$	1344	29(3)	20	
			$27/2^-$	1546	71(3)	80	+0.39
10870	$\star$	$35/2^-$				0.25	
			$31/2^-$	1830	100	100	
10982	$\star$	$33/2^-$				0.04	
			$35/2^-$	*112*	n.o.	0	–0.05
			$29/2^-$	1726	40(3)	10	
			$31/2^-$	1941	60(3)	90	+0.19
12738	$\star$	$37/2^-$				0.04	
			$33/2^-$	1756	42(3)	6	
			$35/2^-$	1868	58(3)	94	+0.19
MLD (keV)						261	
BES (keV)						–610	
MBD						0.159	
B1 and B4, $\pi = +$							
2941	$\star$	$13/2^+$				3.9	
			$9/2^+$	894	100	100	
4081	$\star$	$17/2^+$				1.1	
			$15/2^+$	*703*	n.o.	11	
			$13/2^+$	1140	100	89	
5716	$\star$	$21/2^+$				0.13	
			$17/2^+$	1635	100	6	
			$19/2^+$	*1923*	n.o.	94	
7335	$\star$	$21/2_2^+$				0.01	
			$23/2^-$	*833*	n.o.	0	
			$19/2^-$	*1482*	n.o.	0	
			$21/2^+$	*1619*	n.o.	29	+0.05
			$19/2_2^+$	*1717*	n.o.	0	+0.53
			$17/2_2^+$	*2680*	n.o.	4	
			$17/2^+$	3255	100	57	
			$19/2^+$	*3542*	n.o.	10	+1.8
8214	$\star$	$25/2^+$				0.03	

TABLE IV. (*Continued.*)

E_x (keV)		I_i^π ($\hbar$)	I_f^π ($\hbar$)	E_γ (keV)	$b_{\exp}$	JUN45 τ (ps) b		δ
			$27/2^-$	*503*	n.o.	0		
			$21/2_2^+$	879	33(6)	0		
			$23/2^-$	1712	16(5)	0		
			$21/2^+$	2498	51(7)	53		
			$23/2^+$	*2596*	n.o.	47		–0.01
9483	⋆	$29/2^+$					11	
			$31/2^-$	*443*	n.o.	2		
			$27/2^+$	*805*	n.o.	0		–0.28
			$25/2^+$	1269	43(5)	1		
			$27/2^-$	1773	57(5)	97		
10908	⋆	$33/2^+$					0.38	
			$35/2^-$	*38*	n.o.	0		
			$29/2^+$	1425	39(3)	96		
			$31/2^-$	1867	61(3)	4		
12833	⋆	$37/2^+$					0.12	
			$33/2^+$	1925	84(2)	99		
			$35/2^-$	1963	16(2)	1		
14465	⋆	$41/2^+$					0.41	
			$37/2^+$	1632	100	100		
MLD (keV)							550	
BES (keV)							–717	
MBD							0.354	

imentally unobserved $\pi = +$, $\alpha = -1/2$, structure, and in particular the $19/2^+$ and $23/2^+$ states, considerably below the observed $\pi = +$ $\alpha = +1/2$, structure. Since the previous and the present experimental results were obtained from fusion-evaporation reactions, which populate high-lying states at high spin and then typically approaching and following the yrast line toward the ground state, there is practically no way to have missed such a pronounced yrast $\pi = +$, $\alpha = -1/2$ structure. Furthermore, strong $\Delta I = 1$ branches are predicted, e.g., $21/2^+ \rightarrow 19/2^+$ or $17/2^+ \rightarrow 15/2^+$, in striking variance with former and present experimental observations. In turn, lowering the predicted $\pi = +$, $\alpha = +1/2$ cascade, so that it matches its experimental counterpart, would solve that discrepancy.

The situation is similar for the negative-parity bands B2 and B3, representing opposite signatures. In Fig. 6 one can see that they are reproduced very well *relative* to the predicted B1 structure, i.e., lowering them by about the same amount places the predictions close to experiment. Numerically, this is seen in BES $= -610$ keV in Table IV. The decay pattern of B2 and B3 are in general very well reproduced, in particular the 1772- and 786-keV $E1$ branches at the bottom. The finite $\delta(E2/M1)$ mixing ratios of the $\Delta I = 1$ transition from B3 into B2 are consistent with the measured low DCO values for these transitions (cf. Table I). Only the decay pattern of the 12 738-keV state at the top of B3 is poorly reproduced, leading to a relatively large overall MBD value.

Similarly to B1, also B4 is predicted too high in energy. Furthermore, the lowest two calculated members of B4, i.e., the $21/2_2^+$ level and the $25/2^+$ yrast state, are clearly not members of the observed cascade B4. This is also seen in the predicted lifetime of the $29/2^+$ state, based on too small "in-band" $B(E2)$ values, causing an almost exclusive $E1$ decay from B4 into B2 in the predictions, also at variance with observations.

Experimentally, bands B2, B3, and B4 terminate at spins $35/2^-$, $37/2^-$, and $41/2^+$. In the predictions, the respective next transition is predicted at some 4–6 MeV in energy, i.e., this observed terminating feature is in perfect agreement with the predictions. All in all, with minor adjustments, JUN45 provides a satisfactory description of bands B1 through B4.

B. Cranked Nilsson-Strutinsky calculations

In the following, the observed bands in ^{63}Ga are compared with calculations performed in the cranked Nilsson-Strutinsky formalism [52–54]. The model is based on the rotating modified oscillator potential, where special measures are introduced to label different configurations. Thus, the eigenstates of the potential are classified as belonging to specific j shells or groups of j shells based on the dominant amplitudes in their wave functions. For mass $A \approx 60$ nuclei, an appropriate classification scheme makes it possible to label total configurations as $[(p_1)p_2p_3;(n_1)n_2n_3]$. Here, p_1 (n_1) is the number of proton (neutron) holes in orbitals of $f_{7/2}$ character, p_2 (n_2) the number of particles in the upper fp shell, and p_3 (n_3) the number of $g_{9/2}$ particles. The numbers in parentheses are omitted when equal to zero. For an odd number of particles in a given group, signature can be specified with a subscript "+" for $\alpha = +1/2$ and "−" for $\alpha = -1/2$. For all

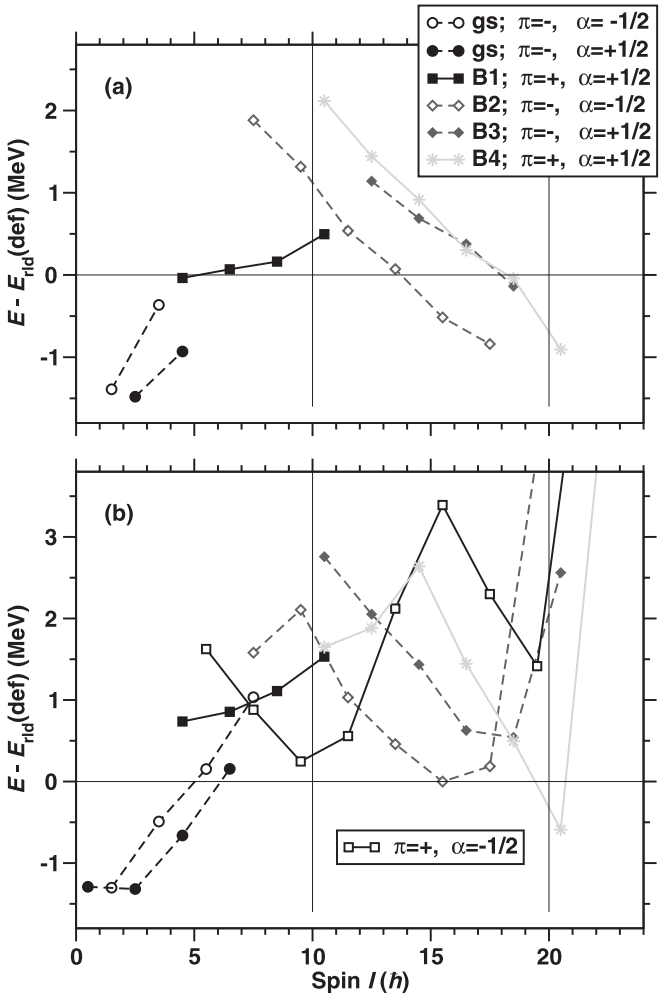

FIG. 6. (a) Excitation energies of the experimental low- to medium spin states labeled gb and B1, B2, B3, and B4 in Fig. 1, respectively. (b) Excitation energies of yrast and a few selected yrare states predicted by shell-model calculations in the $f_{5/2}pg_{9/2}$ model space and the JUN45 interaction [32]. The energies in both panels are plotted relative to a rotating liquid drop energy, $E_{\rm rld}$, calculated according to Ref. [51] (cf. Fig. 7). Structures of positive (negative) parity are connected with full (dashed) lines. Structures with positive (negative) signature, $\alpha = \pm 1/2$, are indicated by filled (open) symbols.

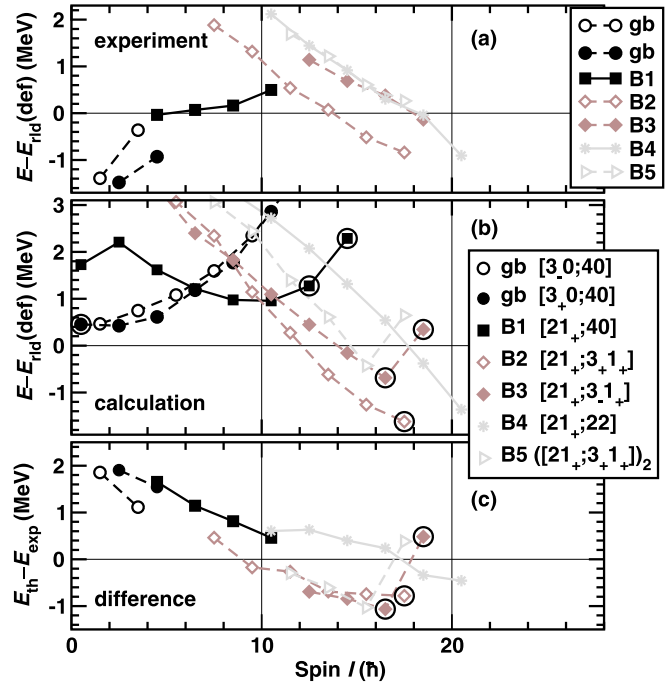

FIG. 7. Comparison between observed and calculated bands in the valence space of ^{63}Ga. In panel (a) the energies of the observed bands are drawn relative to a rotating drop reference [51]. The calculated configurations assigned to these bands are drawn relative to the same reference in panel (b). The difference between experiment and calculations is shown in panel (c). The excited configuration, $([21_+;3_+1_+])_2$, was calculated allowing for all possible excitations. Structures of positive (negative) parity are connected with full (dashed) lines. Structures with positive (negative) signature, $\alpha = \pm 1/2$, are indicated by filled (open) symbols.

configurations considered in this study, $\alpha = 0$ for an even number of particles. The CNS formalism has previously been applied to a large number of nuclei in the $A = 60$ region (see, for instance, Ref. [55] for an overview), as well as for nuclei across the chart of nuclei where high-spin bands are in experimental reach [53]. In the present study we consider only standard parameters [52] (see below).

1. Assessment of the medium-spin bands B1–B5

The observed low- to medium-spin valence space bands of ^{63}Ga are drawn relative to the rotating liquid drop energy in Fig. 7(a). It is evident that the experimental ground-state (gs) bands, shown in Fig. 7(a), are formed with all particles in the fp orbitals. In turn, B1 includes one $g_{9/2}$ particle. Because the Fermi level comes higher for neutrons than for protons, the band lowest in energy of this type comprises one $g_{9/2}$ neutron, i.e., [30;31]. However, the lowest calculated band has signature $\alpha = -1/2$ while the observed band B1 has $\alpha = +1/2$. The lowest calculated band with positive signature sees one $g_{9/2}$ proton, namely [21;40]. Note that this configuration will be favored by like-particle pairing because it has only one "odd particle," contrary to the [30;31] configuration with three "odd particles." Band B1 is thus assigned as $[21_+, 40]$.

The next bands to consider are the (suggested) negative-parity bands B2 and B3. Thus they have to comprise two $g_{9/2}$ particles. The observed bands B2 and B3 are strongly down sloping toward their maximum spin values (cf. Fig. 6). This feature implies that their configurations must have one $g_{9/2}$ proton and one $g_{9/2}$ neutron, because the large signature splitting between the two lowest $g_{9/2}$ orbitals will push configurations with two like $g_{9/2}$ particles, say, [30;22], to a much higher energy and with less down sloping $E - E_{\rm rld}$ curves. Note also that the highest observed spins in bands B2 and B3 nicely correspond to the $I_{\rm max}$ value in the $[21_+; 3_\pm 1_+]$ configurations, namely 17.5 and 18.5, respectively.

To find configurations with higher spin values, i.e., to explain band B4, more particles must be excited to $g_{9/2}$ orbitals or particles can be excited from the $f_{7/2}$ orbitals of the ^{56}Ni

core. However, such holes lead to configurations with less favored high-spin states, i.e., less down sloping $E - E_{\rm rld}$ curves. Thus, the strong down slope of the $E - E_{\rm rld}$ plot for band B4 in Fig. 7(a) implies that its configuration cannot contain any $f_{7/2}$ holes. Hence, because it is observed to $I = 20.5\,\hbar$, it must have at least three $g_{9/2}$ particles, i.e., the only reasonable assignment is the $[21_+; 22]$ configuration. Note that this configuration has positive parity and $I_{\rm max} = (4 + 4.5 + 4 + 8)\,\hbar = 20.5\,\hbar$, corresponding to the highest observed spin in band B4.

In this medium-spin regime, the remaining bandlike structure to investigate is band B5. It is interesting to note that its in-band transition energies are almost identical to those of B2, while the band is positioned ≈ 1.1 MeV higher in energy. Because the band is coming steeply down when drawn relative to the rotating liquid drop energy, very much like bands B2, B3, and B4, it cannot have any holes in the $f_{7/2}$ orbitals. Considering bands with two $g_{9/2}$ particles, i.e., negative parity, calculated bands will be unfavored in energy if one of the $g_{9/2}$ particles is placed in the second lowest $g_{9/2}$ orbital. Thus, the only reasonable configuration has one proton and one neutron in the lowest $g_{9/2}$ orbital, i.e., the configuration $\pi(fp)^2(g_{9/2})^1\nu(fp)^3(g_{9/2})^1$ or $[21_+; 3_+1_+]$, to obtain the proper total signature of band B5, $\alpha = -1/2$. This configuration was, however, already assigned to band B2. This suggests that band B5 is an excited band within the $[21_+; 3_+1_+]$ classification.

With the assignments suggested above, observed and calculated bands are compared in Fig. 7(c). The general agreement is on a similarly good level as in previous studies in the mass region. The differences collected along a down sloping curve are as expected when pairing is neglected. There is one distinct discrepancy in the difference curve though, namely that the highest spin states in specific $\nu(fp)^3$ configurations are calculated too high in energy. This problem can be largely accounted for by lowering the $f_{5/2}$ shell relative to the $p_{3/2}$ shell as illustrated in, for instance, Fig. 24 of the very comprehensive study of the even-even isotone ^{62}Zn [16]. In that figure it is shown how a favored $I = 4.5$ coupling is formed within the partial $\nu(fp)^3$ configuration of band 2 in ^{62}Zn, i.e., with the $m_i = 5/2,\ 3/2$, and $1/2$ states filled. Then, for the signature partner, the $I_{\rm max} = 5.5$ state is formed by lifting the $m_i = 1/2$ particle to the second $m_i = 3/2$ orbital as illustrated by an arrow in that figure. This $\nu(fp)^3$ configuration is not formed from orbitals below a straight-line Fermi surface and is thus much less favored in energy. A similarly unfavored $I_{\rm max}$ state is formed in the second lowest $\nu(fp)^3$ band with signature $\alpha = +1/2$, which is assigned to band B5 of ^{63}Ga. It is formed by lifting the $m_i = 1/2$ neutron to the second lowest $m_i = 1/2$ state. We can thus conclude from Fig. 24 of Ref. [16] that if the $f_{5/2}$ shell was lowered relative to the $p_{3/2}$ shell, the highest spin states in the configurations assigned to bands B3 and B5 would come closer to experiment. Similar examples from bands in ^{62}Zn are presented in Ref. [16]. Indeed, one of the features of the new $A \approx 60$ CNS parameters introduced in Ref. [55] is to put the $f_{5/2}$ and $p_{3/2}$ shells closer, which leads to a better description of a multitude of observed bands. However, another feature of these new parameters is to place the $g_{9/2}$ neutron shell at a lower energy than the $g_{9/2}$ proton shell. This does not seem to be appropriate in view of the general understanding that high-j intruder shells are placed lower for protons than for neutrons because of the Coulomb potential. Therefore, we used the standard parameters in the present description of the ^{63}Ga bands.

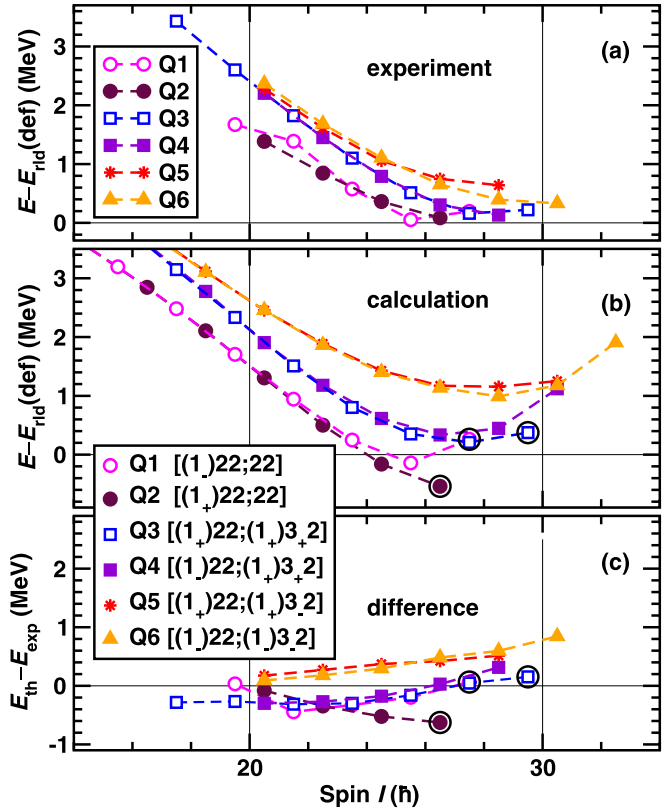

FIG. 8. Comparison between observed high-spin collective bands Q1–Q6, which were linked into the low- and medium-spin level scheme ^{63}Ga, and their calculated counterparts. The bands are drawn into panels (a)–(c) in the same way as in Fig. 7.

2. Assessment of the linked high-spin bands Q1–Q6

The energies of the high-spin bands, which were experimentally linked to the valence-space bands, are drawn relative to the rotating liquid drop energy in Fig. 8(a). The configurations assigned to them are shown in the same manner in Fig. 8(b), and the difference between experiment and calculations can be judged in Fig. 8(c). These differences are nicely collected around zero, suggesting that our assignments are correct. Note, however, that on average the curves in Fig. 8(c) are slightly up sloping. In general one would expect them to be slightly down sloping, considering the neglect of pairing in the CNS calculations.

Bands Q1 and Q2 are close to signature degenerate. This can be expected for configurations with one hole in the $f_{7/2}$ orbitals, which was noticed as early as in the first bands of this type identified in ^{64}Zn [6] and ^{62}Zn [7]. They are thus assigned to the signature partners of the [(1)22,22] configuration, which in fact terminate at the highest observed spin values of Q1 and Q2, namely $I = 26.5$ and 27.5, respectively. The somewhat uneven character of the experimental energy curve of Q1 is

unexpected and different to, for instance, the TB1 and TB2 bands in ^{62}Zn [7,16]. But even so, it is difficult to imagine any alternative assignment for these two bands.

Bands Q3 and Q4 are the bands which are most regular over an extended spin range. They show a pronounced signature degeneracy, suggesting that they comprise one $f_{7/2}$ hole for either protons or neutrons or rather for both protons and neutrons, considering that they are observed to spin values just below spin $I = 30\,\hbar$. Then, because of their negative parity, their configuration consists of an even number of $g_{9/2}$ particles. Therefore, they are compared with the lowest energy $[(1)22;(1)3_+2]$ signature partners in Fig. 8. This interpretation appears convincing, which implies that Q3 is observed to termination and that Q4 is experimentally one transition short of its predicted unfavored termination.

Bands Q5 and Q6 are similar to each other and the states along the bands are close to degenerate according to the suggested experimental spin values and parities. Such a degeneracy would be expected if both protons and neutrons have one $f_{7/2}$ hole in configurations where the signature for both protons and neutrons is switched. For example, this is the case for the two configurations $[(1_+)22;(1_+)3_+2]$ and $[(1_-)22;(1_-)3_-2]$. Consequently, these predictions for these configurations are compared with the experimental bands Q5 and Q6 in Fig. 8. We note that the unfavored signature, $\alpha = -1/2$, is chosen for the fp neutrons because Q3 and Q4 were already assigned to two of the configurations with the favored, $\alpha = +1/2$ signature for these neutrons. The comparison for bands Q5 and Q6 in Fig. 8(c) is satisfactory but leaves room for improvement, considering the increasing trend and the somewhat large positive deviations for the highest spin values. One should also note that the energy degeneracy in the lower spin range is very well fulfilled for the calculated bands but slightly violated in the observed bands. From the theoretical point of view, the Fermi level will appear in a region where the highest $f_{7/2}$ orbitals come close to the next lowest fp orbitals. As discussed in Refs. [16,55], this can complicate the distinction between the fp and $f_{7/2}$ orbitals, which is discussed in connection with, for example, Fig. 28 of Ref. [16]. Consequently, the calculated energies of the configurations assigned to Q5 and Q6 are less precise.

3. Discussion of the high-spin bands Q7, Q8, and Q9

The bands Q7, Q8, and Q9 could not be connected to the observed valence-space structures. This rules any assignment tentative. A further complication in the present case is that the bands with two, three, and four $f_{7/2}$ holes are predicted at a similar energy for spin values around or just below $I = 30\,\hbar$. On the other hand, considering that bands Q7–Q9 are not linked it seems reasonable to assume that they are more different from the valence-space bands B1–B5 than bands Q1–Q6, i.e., that bands Q7–Q9 have to have a larger number of $f_{7/2}$ holes than Q1–Q6. It is then satisfying to see that with the chosen spin values and excitation energies, these bands are well described by configurations with four $f_{7/2}$ holes. This is demonstrated in Fig. 9, where the experimental bands are compared with the two calculated configurations, which are lowest in energy for spin values just beyond $I = 30\,\hbar$ and a third configuration, which is also among those with lowest calculated energy in this spin range.

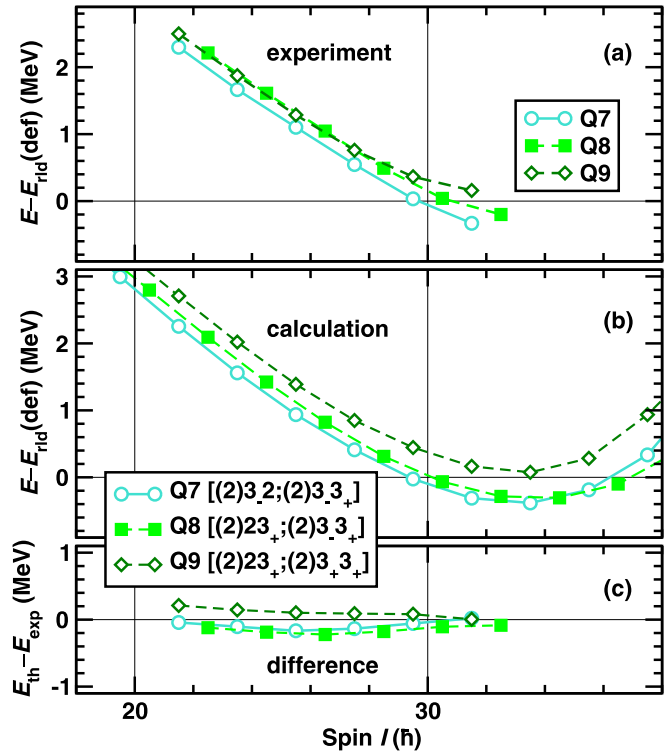

FIG. 9. Comparison between observed bands—Q7, Q8, and Q9—not connected to the main body of the level scheme and the calculated bands in ^{63}Ga. The bands are drawn into panels (a), (b), and (c) in the same way as in Fig. 7.

4. Configuration overview

To obtain a more general understanding of the observed bands in ^{63}Ga, Fig. 10 places the observed bands and their assigned configurations in a scheme depending on the total number of $f_{7/2}$ holes and $g_{9/2}$ particles. A similar figure was

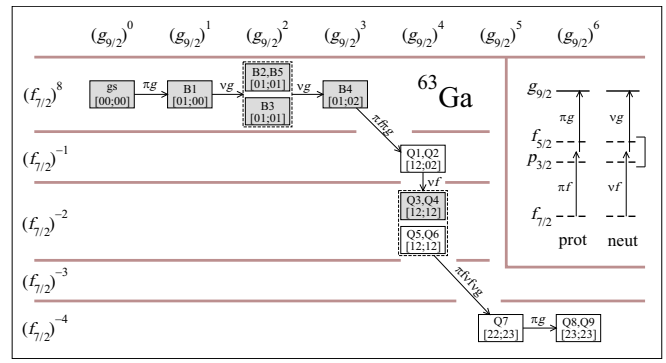

FIG. 10. Classification of the configurations assigned to the observed bands in ^{63}Ga in terms of $f_{7/2}$ holes and $g_{9/2}$ particles. Arrows indicate how the various bands are related through the excitations shown schematically in the inset. The configurations are short labeled as $[p_1p_3;n_1n_3]$, i.e., by the number of proton and neutron holes in $f_{7/2}$ orbitals and particles in $g_{9/2}$ orbitals, respectively. Boxes with well-established configuration assignments are shaded.

constructed for ^{62}Zn [16]. It is interesting that with present assignments, the bands in ^{62}Zn and ^{63}Ga cover the same range of excitations. They start from the ground bands with all particles in the fp orbitals to finally reach configurations of the type $(f_{7/2})^{-4}(g_{9/2})^{6}$. However, while all kinds of intermediate excitations appear to be observed in ^{62}Zn, the number of observed excitations is more limited in ^{63}Ga, most likely reflecting the experimental limitations of lower statistics due to a smaller production cross section.

VI. SUMMARY AND CONCLUSIONS

The level scheme of ^{63}Ga was extended considerably, now comprising more than one hundred γ-ray transitions connection more than 80 excited states. The low-spin part of the level scheme was found to be consistent with previous work, though comparison with theory indicates that a dedicated experimental study is worth conducting to settle some possible inconsistencies. In view of mirror nuclei investigations reaching nuclei beyond ^{56}Ni, it is crucial that the more neutron-rich partner provides a well-established basis or reference. Either a light-ion induced reaction, e.g., ^{58}Ni(^{7}Li, $2n$)^{63}Ga, or a heavy-ion fusion-evaporation near threshold, e.g., ^{40}Ca(^{28}Si, αp)^{63}Ga, with a focus on angular distribution and angular correlation measurements, is suggested.

Such studies would also have the potential to broaden the level scheme, i.e., possibly identify additional near-yrast levels up to some 4 MeV in excitation energy. ^{63}Ga is seemingly a challenge for contemporary but otherwise rather well established shell-model interactions. Thus, the present result, presumably together with complementary, new data on ^{63}Ga and other neighboring nuclei, may help to refine existing shell-model interactions or provide valuable if not decisive input for more comprehensive shell-model spaces such as, e.g., $fpg_{9/2}$ or $fpg_{9/2}d_{5/2}$.

The medium-spin ($I \approx 10$ to $18\,\hbar$) and excitation energy ($E_x \approx 5$ to 14 MeV) part of the ^{63}Ga was partially revised and grouped into four bandlike structures, which find consistent explanations both from a shell-model point of view as well as cranked Nilsson-Strutinsky calculations. This provides confidence to the firmly and tentatively assigned spins and parities of the corresponding states.

A total of nine rotational bands were observed at high spins ($I > 20\,\hbar$) and excitation energies ($E_x > 15$ MeV), six of which could be connected by high-energy linking transitions to the previously known part of the level scheme. They find their explanation in an increasing number of holes generated in the $f_{7/2}$ orbitals below ^{56}Ni, in combination with an increasing number of particles in the deformation driving $g_{9/2}$ orbitals. Complementing Fig. 10 as well as attempting to drive the level scheme of ^{63}Ga to new heights in spin and energy, like for some neighboring nuclei [56,57], poses a challenge for the new generation of germanium tracking arrays.

ACKNOWLEDGMENTS

We thank the accelerator crews and the Gammasphere support staff at Argonne and for their supreme efforts. This research used resources of ANL's ATLAS facility, which is a DOE Office of Science User Facility. This work is supported in part by the Swedish Research Council (Vetenskapsrådet, VR 2016-3969) and the U.S. Department of Energy under Grants No. DE-AC02-06CH11357 (ANL), No. DE-AC02-05CH11231 (LBNL), and No. DE-FG05-88ER-40406 (WU). D.R. thanks Silvia Lenzi, Padova, for discussions and support concerning the ANTOINE shell-model calculations.

[1] A. Poves, J. Sánchez-Solano, E. Caurier, and F. Nowacki, Nucl. Phys. A **694**, 157 (2001).
[2] M. Honma, T. Otsuka, B. A. Brown, and T. Mizusaki, Phys. Rev. C **65**, 061301(R) (2002).
[3] E. Caurier, G. Martińez-Pinedo, F. Nowack, A. Poves, and A. P. Zuker, Rev. Mod. Phys. **77**, 427 (2005).
[4] J. Ekman, C. Fahlander, and D. Rudolph, Mod. Phys. Lett. A **20**, 2977 (2005).
[5] M. A. Bentley and S. M. Lenzi, Prog. Part. Nucl. Phys. **59**, 497 (2007).
[6] A. Galindo-Uribarri, D. Ward, G. C. Ball, V. P. Janzen, D. C. Radford, I. Ragnarsson, and D. Headly, Phys. Lett. B **422**, 45 (1998).
[7] C. E. Svensson *et al.*, Phys. Rev. Lett. **80**, 2558 (1998).
[8] A. V. Afanasjev, I. Ragnarsson, and P. Ring, Phys. Rev. C **59**, 3166 (1999).
[9] D. Rudolph *et al.*, Phys. Rev. Lett. **82**, 3763 (1999).
[10] D. Rudolph *et al.*, Phys. Rev. Lett. **80**, 3018 (1998).
[11] C. E. Svensson *et al.*, Phys. Rev. Lett. **82**, 3400 (1999).
[12] E. K. Johansson *et al.*, Phys. Rev. C **80**, 014321 (2009).
[13] C. Andreoiu *et al.*, Eur. Phys. J. A **14**, 317 (2002).
[14] L.-L. Andersson *et al.*, Eur. Phys. J. A **36**, 251 (2008).
[15] L.-L. Andersson *et al.*, Phys. Rev. C **79**, 024312 (2009).
[16] J. Gellanki *et al.*, Phys. Rev. C **86**, 034304 (2012).
[17] P. J. Ennis, C. J. Lister, W. Gelletly, H. G. Price, B. J. Varley, P. A. Butler, T. Hoaer, S. Cwiok, and W. Nazarewicz, Nucl. Phys. A **535**, 392 (1991).
[18] U. Hermkens, F. Becker, T. Burkardt, J. Eberth, S. Freund, T. Mylaeus, S. Skoda, W. Teichert, H. G. Thomas, and A. v. d. Werth, Phys. Rev. C **52**, 1783 (1995).
[19] W. Nazarewicz, J. Dudek, R. Bengtsson, T. Bengtsson, and I. Ragnarsson, Nucl. Phys. A **435**, 397 (1985).
[20] P. H. Heenen, P. Bonche, J. Dobaczewski, and H. Flocard, Nucl. Phys. A **561**, 367 (1993).
[21] A. Petrovici, K. W. Schmid, and A. Faessler, Nucl. Phys. A **605**, 290 (1996).
[22] J. Heese, K. P. Lieb, L. Lühmann, F. Raether, B. Wörmann, D. Alber, H. Grawe, J. Eberth, and T. Mylaeus, Z. Phys. A **325**, 45 (1986).
[23] T. Mylaeus *et al.*, J. Phys. G: Nucl. Part. Phys. **15**, L135 (1989).
[24] S. M. Fischer, C. J. Lister, and D. P. Balamuth, Phys. Rev. C **67**, 064318 (2003).

[25] B. J. Varley, M. Campbell, A. A. Chisti, W. Gelletly, L. Goettig, C. J. Lister, A. N. James, and Ö. Skeppstedt, Phys. Lett. B **194**, 463 (1987).
[26] H. Iwasaki *et al.*, Phys. Rev. Lett. **112**, 142502 (2014).
[27] E. Stiliaris, H. G. Bohlen, X. S. Chen, B. Gebauer, A. Miczaika, W. von Oertzen, W. Weller, and T. Wilpert, Z. Phys. A **326**, 139 (1987).
[28] D. Rudolph, D. Weisshaar, F. Cristancho, J. Eberth, C. Fahlander, O. Iordanov, S. Skoda, Ch. Teich, O. Thelen, and H. G. Thomas, Eur. Phys. J. A **6**, 377 (1999).
[29] D. P. Balamuth, U. J. Hüttmeier, T. Chapuran, D. G. Popescu, and J. W. Arrison, Phys. Rev. C **43**, 2082 (1991).
[30] M. Weiszflog *et al.*, Eur. Phys. J. A **11**, 25 (2001).
[31] T. F. Lang, D. M. Moltz, J. E. Reiff, J. C. Batchelder, J. Cerny, J. D. Robertson, and C. W. Beausang, Phys. Rev. C **42**, R1175(R) (1990).
[32] M. Honma, T. Otsuka, and T. Mizusaki, and M. Hjorth-Jensen, Phys. Rev. C **80**, 064323 (2009).
[33] L.-L. Andersson, E. K. Johansson, J. Ekman, D. Rudolph, R. du Rietz, C. Fahlander, C. J. Gross, P. A. Hausladen, D. C. Radford, and G. Hammond, Phys. Rev. C **71**, 011303(R) (2005).
[34] B. Erjun and H. Junde, Nucl. Data Sheets **92**, 147 (2001).
[35] H. Junde, Y. Dong, H. Meirong, ENSDF (cut-off date 28-Aug-2008), http://www.nndc.bnl.gov/ensdf.
[36] T. J. Procter *et al.*, Phys. Rev. C **86**, 034329 (2012).
[37] T. W. Henry, Mirror & Triplet spectroscopy in the fp shell with SeGA and GRETINA, Ph.D. thesis, University of York, 2015.
[38] D. Rudolph *et al.*, Phys. Rev. C **102**, 014313 (2020).
[39] I.-Y. Lee, Nucl. Phys. A **520**, 641c (1990).
[40] M. Devlin, L. G. Sobotka, D. G. Sarantites, and D. R. LaFosse, Nucl. Instrum. Methods A **383**, 506 (1996).
[41] D. G. Sarantites, P.-F. Hua, M. Devlin, L. G. Sobotka, J. Elson, J. T. Hood, D. R. LaFosse, J. E. Sarantites, and M. R. Maier, Nucl. Instrum. Methods A **381**, 418 (1996).
[42] C. E. Svensson *et al.*, Nucl. Instrum. Methods A **396**, 228 (1997).
[43] D. C. Radford, Nucl. Instrum. Methods A **386**, 297 (1995).
[44] J. Theuerkauf, S. Esser, S. Krink, M. Luig, N. Nicolay, O. Stuch, and H. Wolters, program TV, University of Cologne (unpublished).
[45] E. Caurier, shell model code ANTOINE, IRES, Strasbourg 1989–2002.
[46] F. Nowacki and E. Caurier, Acta Phys. Pol. B **30**, 749 (1999).
[47] W. A. Richter, M. G. van der Merwe, R. E. Julies, and B. A. Brown, Nucl. Phys. A **523**, 325 (1991).
[48] R. du Rietz *et al.*, Phys. Rev. Lett. **93**, 222501 (2004).
[49] D. Rudolph, K. P. Lieb, and H. Grawe, Nucl. Phys. A **597**, 298 (1996).
[50] T. Mizusaki, K. Kaneko, and M. Hasegawa, Acta Phys. Pol. B **38**, 1363 (2007).
[51] K. Pomorski and J. Dudek, Phys. Rev. C **67**, 044316 (2003).
[52] T. Bengtsson and I. Ragnarsson, Nucl. Phys. A **436**, 14 (1985).
[53] A. V. Afanasjev, D. B. Fossan, G. J. Lane, and I. Ragnarsson, Phys. Rep. **322**, 1 (1999).
[54] B. G. Carlsson and I. Ragnarsson, Phys. Rev. C **74**, 011302(R) (2006).
[55] J. Gellanki, B. G. Carlsson, I. Ragnarsson, and D. Rudolph, Phys. Rev. C **89**, 024301 (2014).
[56] D. Rudolph *et al.*, Phys. Rev. Lett. **96**, 092501 (2006).
[57] J. Gellanki *et al.*, Phys. Rev. C **80**, 051304(R) (2009).